8-10-2018

Analytical Models of Neutron Spectral Fluence, Kerma and Absorbed-Dose for Proton Therapy

Suman Shrestha
Louisiana State University and Agricultural and Mechanical College

ANALYTICAL MODELS OF NEUTRON SPECTRAL FLUENCE, KERMA AND ABSORBED-DOSE FOR PROTON THERAPY

A Thesis

Submitted to the Graduate Faculty of the
Louisiana State University and
Agricultural and Mechanical College
in partial fulfillment of the
requirements for the degree of
Master of Science

in

The Department of Physics and Astronomy

by
Suman Shrestha
B.Sc., Tribhuvan University, 2010
M.Sc., Tribhuvan University, 2013
December 2018

Acknowledgements

My sincerest gratitude goes to my advisor, Dr. Wayne Newhauser, for the opportunity to work with and learn from him. I wholeheartedly appreciate his guidance and support over the course of this research. I also thank Dr. Kenneth Matthews for his guidance and support over the course of my time in the program. I also thank my committee members, Drs. Joyoni Dey, Abbie Wood, Angelica Perez-Andujar and Daniel Sheehy, for investing their time and expertise.

I would like to acknowledge all faculty and staff involved with the medical physics program at Louisiana State University (LSU) and Mary Bird Perkins Cancer Center. I appreciate the professors and thank them for guidance with my studies.

I also want to thank all my student colleagues I have known in my time at LSU for their camaraderie. Specifically, acknowledge my fellow classmates Elizabeth Hilliard, Addie Barron and Jingzhu Xu for helping me navigate through graduate studies. Additionally, I would like to thank William Donahue for his invaluable suggestions during my time at LSU.

Finally, I am who I am and where I am because of my family. I thank my father, mother and brother for their unwavering love and support, who have always been and will always be my biggest sources of motivation and inspiration.

Table of Contents

Acknowledgements ii

List of Tables iv

List of Figures v

Abstract vi

Chapter 1. Introduction 1

Chapter 2. Methods and Materials 5
2.1. Kerma and Absorbed Dose 5
2.2. Model for Kerma Coefficient 6
2.3. Analytical Model for Neutron Spectral Fluence 8
2.4. Kerma Calculation 17
2.5. Absorbed-Dose Calculation 17

Chapter 3. Results 19
3.1. Empirical Model of Kerma Coefficient 19
3.2. Analytical Model of Neutron Spectral Fluence 21
3.3. Neutron Kerma Calculation 29
3.4. Absorbed-Dose Calculation 31

Chapter 4. Discussion 35

Chapter 5. Conclusion 38

References 39

Vita 43

List of Tables

Table 3.1. Parameters from fitting neutron kerma coefficient values to proposed analytical model..... 19

Table 3.2. Average and maximum relative difference in neutron kerma coefficients between data from ICRU Report 63 and the analytical model. 20

Table 3.3. Parameters governing neutron spectral fluence, neutron attenuation factor, and off-axis factor..... 22

Table 3.4. Parameters for modeling dependence of neutron spectral fluence on proton beam energy..... 22

Table 3.5. Fluence-weighted average neutron energy and fluence-weighted average kerma coefficient, including relative difference for 180-MeV proton beams 27

Table 3.6. Average relative difference and maximum relative difference between average energy values calculated by Monte Carlo method and analytical model..... 28

Table 3.7. Average relative difference and maximum relative difference between average kerma coefficient values calculated by Monte Carlo method and analytical model 29

Table 3.8. Select examples of neutron kerma and relative difference for 120-MeV and 250-MeV proton beams from analytical model and Monte Carlo simulations..... 30

Table 3.9. Average relative difference and maximum relative difference between absorbed-dose values calculated by Monte Carlo method and the analytical model. 34

List of Figures

Figure 1.1. Schematic diagram representing a treatment head and patient treated..... 2

Figure 2.1. Neutron energy fluence spectrum from proton therapy illustrating contributions from separate energy regimes..... 10

Figure 2.2. Geometry of a general-purpose proton treatment head and water phantom. Adapted from Perez-Andujar et al. (2013)..... 12

Figure 3.1. Neutron kerma coefficient *versus* neutron energy in water..... 20

Figure 3.2. Selected examples of neutron spectral fluence at isocenter produced by 120 to 250-MeV proton beams. These were calculated using the analytical model [Eq. (10)]..... 21

Figure 3.3. Selected examples of neutron spectral fluence at 22-cm and 40-cm water depth along central axis produced by 180-MeV proton beams..... 23

Figure 3.4. Selected examples of neutron spectral fluence at 22-cm and 40-cm water depth along 80 cm off-axis distance produced by 180-MeV proton beams..... 24

Figure 3.5. Predication of kerma contribution from Monte Carlo (red) and analytical model (blue) *versus* neutron energy..... 25

Figure 3.6. Selected example predictions from Monte Carlo (points) and analytical model (lines) of neutron fluence *versus* depth..... 26

Figure 3.7. Selected example predictions from Monte Carlo (points) and analytical model (lines) of neutron fluence *versus* off-axis position..... 26

Figure 3.8. Variation of average neutron energy with off-axis distance and depth for 120-MeV, 180-MeV and 250-Mev proton beam..... 29

Figure 3.9. Predicted kerma, *K*, from Monte Carlo (points) and analytical model (lines) of kerma *versus* off-axis position..... 30

Figure 3.10. Comparison of absorbed-dose, *D*, and kerma, *K*, calculated using MC data *versus* off-axis distance x..... 31

Figure 3.11. Kerma-to-absorbed dose conversion factor *versus* off-axis distance..... 32

Figure 3.12. Predictions of absorbed dose, *D*, from analytical model (lines) and Monte Carlo calculation (points) *versus* off-axis distance..... 33

Figure 3.13. Prediction of absorbed dose, *D*, from analytical model (lines) and Monte Carlo calculation (points) *versus* depth in water..... 34

Abstract

Purpose: The accurate prediction of stray neutron dose has become increasingly important as it increases the risk of second cancer development after proton therapy. Previously reported analytical models predicted the quantity dose equivalent, which includes physical and biological considerations but does not explicitly take into account material dependence and variation in the radiation quality. The purpose of this study was to investigate the feasibility of an analytical model of absorbed dose to water from stray neutrons in proton therapy.

Methods: To calculate neutron absorbed dose and kerma in water, the authors developed analytical models of neutron spectral fluence and kerma coefficients, used neutron spectral fluence and absorbed dose data from Monte Carlo simulations, and evaluated neutron kerma coefficients from the literature.

Results: The analytical model predictions of absorbed dose to water agreed relatively well with that from Monte Carlo simulations. On average, the percentage difference between the analytical model and Monte Carlo simulations was 49 percent for absorbed dose to water for the proton beam energies ranging from 120 MeV to 250 MeV.

Conclusion: The results suggest that it is feasible to analytically model absorbed dose to water from stray neutrons with good accuracy. A potentially important advantage of this fluence-based approach is that it provides the ability to take material dependence into account and helps with characterization of radiation quality.

Chapter 1. Introduction

Cancer is one of the most significant health issue in the developed world. Approximately one in two men and women will be diagnosed with some form of cancer in their lifetime (Howlader et al. 2014). With advancements in cancer care the 5-year survival rate is now 83% averaged overall for all cancers (Siegel et al. 2018) and the number of cancer survivors in United States is expected to increase from 15.5 million in 2016 to 20.3 million by 2026 (DeSantis et al. 2014, Siegel et al. 2018). Nearly two thirds of all cancer patients will receive radiation therapy at some point during their treatment (Smart 2010).

Radiation-induced late effects, such as cardiac toxicity, second cancers, and fertility complications, are prevalent in these cancer survivors (NRC 2006, NCRP 2011, Williams et al. 2018). With increasing survival, it has become essential to understand the mechanism behind these complications in an attempt to mitigate against them and improve the quality of life for cancer survivors.

Childhood cancer survivors who received radiation therapy are at elevated risk for health complications, with a 2.5 times increased risk of developing a second cancer when compared to their healthy siblings (Tukenova et al. 2010). Modern radiation therapy techniques, such as proton therapy, seek to avoid radiation side effects by delivering a highly conformal dose to the tumor. However, normal tissues outside the treatment field are unavoidably exposed to considerable levels of scattered and leakage radiation (Figure 1.1). Most secondary malignancies in adults occur outside the primary field (Doerr et al. 2002, Diallo et al. 2009) implicating stray radiation exposures. Therefore, accurate prediction of stray dose will become increasingly important for understanding and avoiding radiogenic second cancers.

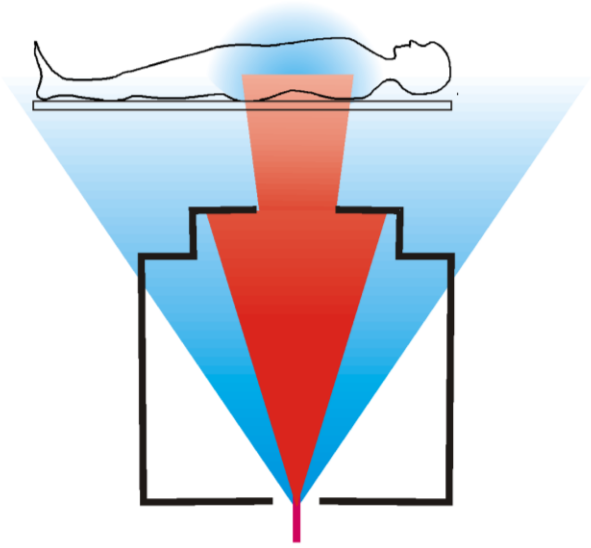

Figure 1.1. Schematic diagram representing a treatment head and patient treated. Therapeutic radiation beam is shown in red while blue represents stray radiation incident upon patient's whole body (Newhauser et al. 2011).

Proton therapy provides uniform target coverage and lower dose to normal tissue than photon therapy. However, patients undergoing proton therapy still receive stray radiation dose, primarily from neutrons that are generated in treatment head and the patient's body (Figure 1.1). These neutrons are created through various physical processes such as direct reactions, pre-compound emission, compound emission, etc. Theoretically the risk of secondary cancer after proton therapy is significantly lower than that after photon therapy, but epidemiologic evidence is lacking.

Measurements of the neutron fields generated during proton therapy have provided critical insights. Yan et al. (2002) measured the neutron dose equivalent outside the treatment field and demonstrated the existence of a neutron bath from three proton-therapy beamlines. Since then, numerous researchers have reported measurements of secondary neutron dose for a proton-

therapy beamline, which were selectively reviewed in NCRP (2011). Tayama et al. (2006) validated Monte-Carlo codes using measurements of neutron yield for various proton energies. Measurements are essential for developing (Schneider et al. 2015) and validating (Farah et al. 2015) analytical models of both therapeutic and stray dose. Recently myriad measurement-based studies has been published for pencil beam scanning (Islam et al. 2017, Trinkl et al. 2017) as well as passive-scattering (Howell et al. 2016, De Smet et al. 2017) proton beamlines. Measurements are technically challenging and time consuming.

Monte Carlo simulations allow researchers to determine in-field and out-of-field neutron dose for arbitrary geometries and treatment modalities. Though extremely insightful, the long computation times and complexity of MC simulations has limited its application to research settings. Agosteo et al. (1998) first utilized MC methods to simulate dose from secondary neutrons and photons from an ocular proton treatment. In addition to the quantities provided by basic measurements, it is possible to determine and discriminate the source of the particles, which can be used to develop analytical models. These advantages led to increasing literature of neutron exposure simulated with MC techniques (Newhauser et al. 2002, Hongyu et al. 2005, Zheng et al. 2008, Perez-Andujar et al. 2013, Zhang et al. 2013). This approach has been applied to both active scanning (Trinkl et al. 2017) and passive (Farah et al. 2015, Bonfrate et al. 2016) beamlines. Data generated by MC are being used for the training and validation of analytical models.

To develop methods suitable for routine clinical calculations of absorbed dose, several research groups have proposed analytical models. An early attempt to analytically model neutron dose was reported by Polf et al. (2005). Anferov (2010) proposed an analytical model for converting proton beam losses into secondary-neutron dose. Newhauser et al. (2017) presented a concise review of recent analytical models and their efficacy and concluded that these may offer

faster computations of equivalent dose with acceptable accuracy. Another such model has been developed by Newhauser and co-workers over the past decade. It is nonproprietary and straightforward to implement. Basic versions of these analytical models were developed between 2006 and 2010 at The University of Texas MD Anderson Cancer Center (Zhang et al. 2010) and advanced versions between 2011 and 2017 at Louisiana State University with collaborators from Mary Bird Perkins Cancer Center and other institutions (Perez-Andujar et al. 2013, Eley et al. 2015, Farah et al. 2015, Schneider et al. 2015). This model estimates equivalent dose per prescribed proton absorbed dose in water phantom. The recent version reported by Schneider et al. (2015) was simpler to configure and use than previously version and offered continuous applicability from 100-250 MeV in proton beam energy. Eley et al. (2015) integrated this model into a treatment planning system and extended the model to include range modulation and arbitrary collimator shapes. Gallagher et al. (2018) performed an independent application and evaluation of this model in clinically realistic circumstances and demonstrated that analytical models may be useful for clinicians and researchers to calculate equivalent dose. As explained, previous models have predicted the quantity dose equivalent, which was developed for radiation protection purposes and includes an amalgamation of physical and biological considerations. However, this approach is limited in that it does not take into account material dependence (e.g., muscle versus bone) and does not allow characterization of radiation quality.

The objective of this study was to investigate the feasibility of an analytical model of absorbed dose to water from stray neutrons in proton therapy. The model calculates neutron spectral fluence, kerma coefficients, kerma, absorbed dose, and mean neutron energy.

Chapter 2. Methods and Materials

2.1 Kerma and Absorbed Dose

The interactions of neutrons in matter depends upon their energy and material composition. Low energy neutrons in tissue mostly undergo neutron capture by nitrogen or hydrogen whereas intermediate and fast neutrons mostly interact through elastic scattering on hydrogen nuclei. Very fast neutrons can undergo non-elastic nuclear reactions with a nucleus or one or more nucleons in a nucleus.

The kerma (K) for neutrons is given by

$$K = \frac{\mathrm{d}\epsilon_{\mathrm{tr}}}{\mathrm{d}m} \tag{1}$$

where $\mathrm{d}\epsilon_{tr}$ is the mean sum of the initial kinetic energy of all the charged particles liberated in the mass $\mathrm{d}m$ of a material by the neutrons incident on $\mathrm{d}m$.

Due to radiative losses and escaping charged particles, not all of the energy is deposited locally, *i.e.*, at the incident neutron's original point of interaction. The absorbed dose (D) is given by

$$D = \frac{\mathrm{d}\epsilon}{\mathrm{d}m} \tag{2}$$

where $\mathrm{d}\epsilon$ is the expectation value of energy imparted to matter of mass $\mathrm{d}m$.

Kerma and absorbed dose are related. The value of the kerma approaches that of the absorbed dose to the degree that charged particle equilibrium (CPE) exists, that radiative losses are negligible. CPE exists at a point if charged-particle fluence rate, differential in energy and direction, is constant within distances equal to the maximum charged-particle range (ICRU 2000,

ICRU 2014). Under conditions of CPE each charged particle of a given type and energy leaving the volume is replaced by identical particle of same energy entering in-terms of their expectation values, *i.e.*,

$$\epsilon_{\mathrm{tr}} \overset{\mathrm{CPE}}{=} \epsilon \tag{3}$$

Thus, the absorbed dose is equal to kerma, or

$$D \overset{\mathrm{CPE}}{=} K \tag{4}$$

In polyenergetic fields kerma is,

$$K = \int_0^{E_{\mathrm{n,max}}} \Phi(E_{\mathrm{n}}) \;\; k_{\phi}(E_{\mathrm{n}}) \; \mathrm{d}E_{\mathrm{n}} \tag{5}$$

where $\Phi(E_{\mathrm{n}})$ is the neutron spectral fluence, $k_{\phi}(E_{\mathrm{n}})$ is kerma coefficient and E_{n} is neutron energy. Thus, substituting Equation (4) in Equation (5), we have

$$D \overset{\mathrm{CPE}}{=} K = \int_0^{E_{\mathrm{n,max}}} \Phi(E_{\mathrm{n}}) \;\; k_{\phi}(E_{\mathrm{n}}) \; \mathrm{d}E_{\mathrm{n}} \tag{6}$$

This expression is very useful because with knowledge of the neutron spectral fluence and kerma coefficients, we can calculate kerma and, under condition of CPE, the absorbed dose.

2.2 Model for Kerma Coefficient

The kerma coefficient, $k_{\phi}(E_{\mathrm{n}})$, or fluence-to-kerma conversion coefficient, is the quotient of the kerma at a given point in a material by the fluence of uncharged ionizing particles, Φ, at the same point, or

$$k_{\phi} = \frac{K}{\Phi} \tag{7}$$

The kerma coefficient may also be calculated from the microscopic cross sections according to

$$k_{\phi}(E_{\mathrm{n}}) = \sum_{\mathrm{j}} N_{\mathrm{j}} \sum_{i} \bar{\epsilon}_{\mathrm{ij}}(E_{\mathrm{n}}) \ \sigma_{\mathrm{ij}}^{\mathrm{prod}}(E_{\mathrm{n}}) \tag{8}$$

where N_{j} denotes the number of target nuclides of type j per unit mass in the material, $\bar{\epsilon}_{\mathrm{ij}}$ the average energy transferred to kinetic energy of charged particles of type i, and $\sigma_{\mathrm{ij}}^{\mathrm{prod}}(E_{\mathrm{n}})$ the total production cross section for a charged particle of type i.

Neutron kerma coefficients are well known below 20 MeV and, with larger uncertainties, between 20 MeV and 150 MeV. At higher neutron energies, information on microscopic cross sections and evaluated kerma coefficient is uncertain and incomplete (ICRU 2000).

2.2.1 Analytical Model of Neutron Kerma Coefficient

In this study we propose the following piecewise formula for neutron kerma coefficients

$$k_{\phi}(E_{\mathrm{n}}) = a_1 \ \cosh(\mathrm{Log}(E_{\mathrm{n}})) + \ H\left(E_{\mathrm{n,Thresh}} - E_{\mathrm{n}}\right) \ \frac{b_1}{\sqrt{2\pi}\sigma_1{}'} \ e^{\left(\frac{-(\mathrm{Log}(E_{\mathrm{n}})-\mu_1)^2}{2\sigma_1'^2}\right)} + H\left(E_{\mathrm{n}} - E_{\mathrm{n,Thresh}}\right) \ \left(u\,{E_{\mathrm{n}}}^2 + v\right) \tag{9}$$

where H is the Heaviside function, E_{n} is neutron energy, and $E_{\mathrm{n,Thresh}}$ is the neutron threshold energy that determines the energy interval covered by each of the two higher energy terms. a_1, b_1, $\sigma_1{}'$, μ_1, u and v are empirical parameters whose values are obtained by fitting Equation (9) to tabulated kerma coefficient data. Equation (9) uses a hyperbolic cosine function for thermal regions, log-normal distribution below $E_{\mathrm{n,Thresh}}$ and second order polynomial to model kerma coefficient at higher energies.

2.2.2 Kerma Coefficient Data for Fitting

We fitted Equation (9) to evaluated kerma coefficient data from ICRU (2000) (ICRU Report 63). The models and experimental data used to derive the evaluated data tables were described by the ICRU (2000). We fitted kerma coefficient data for water, bone, air, muscle, TE-Methane, TE-Propane, A150 tissue substitute plastic, over the interval of 2.53×10^{-8} MeV to 150 MeV neutron energy.

2.2.2 Fitting Procedure

Fitting was performed using a non-linear least squares method and trust-region algorithm implemented in commercial software (MATLAB® and Curve Fitting Toolbox 3.5.6, 2017b, The MathWorks Inc., Natick, Massachusetts, United States). To assess goodness of fit, average and maximum differences between analytical model and evaluated kerma coefficient data were reported.

2.3 Analytical Model for Neutron Spectral Fluence

2.3.1 Analytical Model

Neutrons emitted during proton therapy span about twelve decades of energy. Following the approach from our group (Perez-Andujar et al. 2013, Schneider et al. 2015), we subdivided the spectra into four neutron energy regimes (intranuclear cascade, evaporation, $1/E_{\mathrm{n}}$ and thermal), as shown in Figure 2.1.

A fast proton may penetrate the coulomb barrier of an atomic nucleus. Once inside, it may interact directly with one or a few nucleons, resulting in their emission, usually in the cone of the forward direction due to the principle of conservation of energy. These are called cascade neutrons or direct neutrons. The incident proton may interact with many nucleons in the nucleus,

thus sharing the kinetic energy amongst them. As this process of sharing proceeds, the energy is statistically distributed, eventually reaching an equilibrium where the nucleus is in an excited state. After equilibration, the compound nucleus comprises the original nucleus and the incident proton. The nucleus can de-excite by evaporating off one or more of its nucleons, in a manner that is analogous to the evaporation of water, which is sometimes called compound emission. Nucleons may be emitted during the equilibration process, which is called pre-equilibrium emission. The third energy regime, $1/E_{\mathrm{n}}$ neutrons, correspond to neutrons that have lost some portion of their energy via inelastic scattering, a process referred to as moderation. A small proportion of these neutrons will be lost via capture processes. Finally, the lowest energy regime corresponds to moderated neutrons that have lost most of their kinetic energy and are in thermal equilibrium with the environment. These undergo elastic scattering until they are eventually captured, e.g. by hydrogen and nitrogen nuclei in the material. The emission of evaporation neutrons, $1/E_{\mathrm{n}}$ neutrons and thermal neutrons is isotropic in nature due to loss of directionality information during the equilibration process.

The analytical model for neutron spectral fluence at any point $p(x, y, z)$ in a water phantom is given by

$$\Phi(E_{\mathrm{n}}) = F_{E_{\mathrm{p}}} \; F_{\mathrm{Div}} \; \sum_{i=1}^{4} [AF_{\mathrm{i}} \;\; OAF_{\mathrm{i}} \;\; \phi_{\mathrm{i}}(E_{\mathrm{n}})] \tag{10}$$

where $F_{E_{\mathrm{p}}}$ is proton energy scaling factor that characterizes the dependence of magnitude of neutron fluence on proton beam energy and is given by,

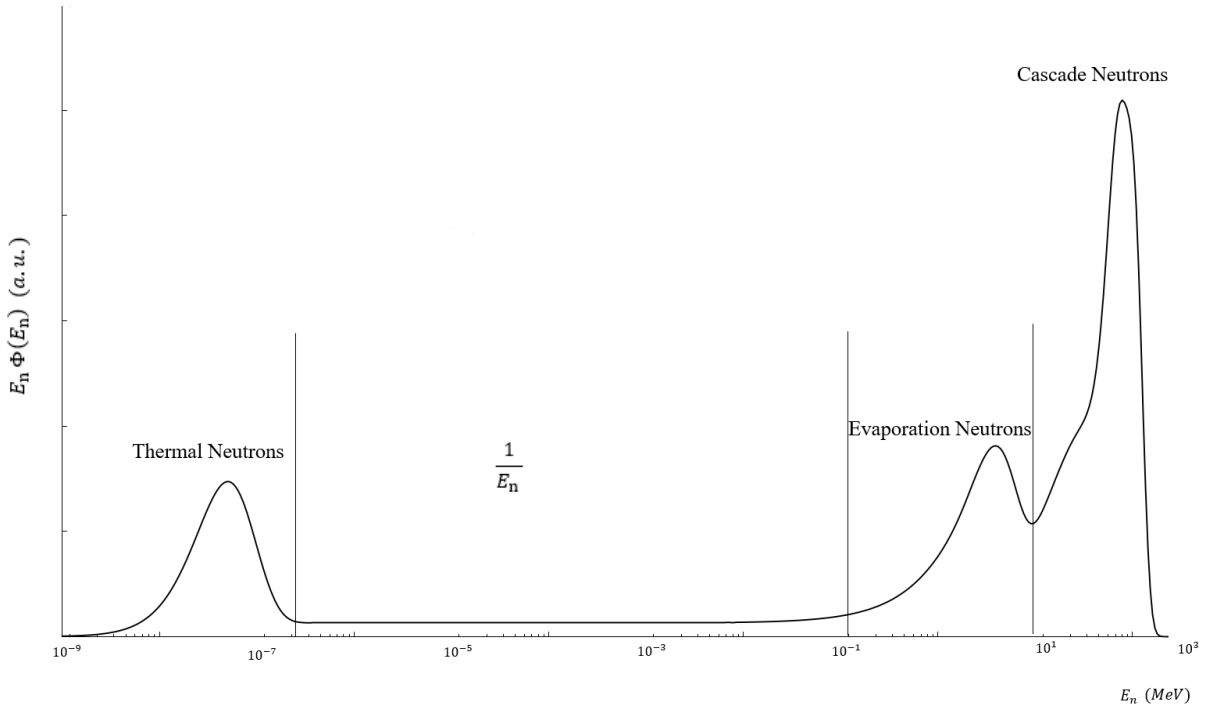

Figure 2.1. Neutron energy fluence spectrum from proton therapy illustrating contributions from separate energy regimes.

$$F_{E_\mathrm{p}} = \alpha_\mathrm{E} \left(\frac{E_\mathrm{p}}{E_\mathrm{p,ref}}\right)^{\xi} \tag{11}$$

where α_E is a constant and ξ is an exponent governing the power law dependence in proton energy, E_p is proton energy and, $E_\mathrm{p,ref}$ is a reference proton energy. Both α_E and ξ are empirical fit parameters. In this work, $E_\mathrm{p,ref}$ was 120 MeV. In this work, spectral fluence and fluence are normalized per proton entering the treatment head.

F_Div denotes the neutron fluence-divergence factor, or

$$F_\mathrm{Div} = \left[\frac{d}{d_\mathrm{iso}}\right]^{-\tau} \tag{12}$$

where d is distance from the effective neutron source to calculation point $p(x, y, z)$ (Figure 2.2), d_{iso} is the distance from the effective neutron source to isocenter (Figure 2.2), and the exponent τ governs the rate of divergence of the source.

The effective attenuation factor (AF_{i}) of neutrons in water is given by

$$AF_{\mathrm{i}} = e^{-\alpha_{\mathrm{i}}[d' - d'_{\mathrm{iso}}]} \tag{13}$$

where α_{i} is the effective attenuation coefficients for the i^{th} neutron energy regime, d'_{iso} is the distance from phantom surface to the isocenter (Figure 2.2), and d' is the distance from the surface to the calculation point along the ray (Figure 2.2).

The off-axis factor (OAF_{i}) describes the lateral distribution of neutron fluence and is given by the normalized gaussian

$$OAF_{\mathrm{i}} = \frac{(d_{\mathrm{iso}})^2}{2\pi\,(\sigma_{\mathrm{i}} z)^2} \quad e^{-\left[\frac{(x^2+y^2)d_{\mathrm{iso}}^2}{2\sigma_{\mathrm{i}}^2 z^2}\right]} \tag{14}$$

where, σ_{i} is the gaussian width parameter of the i^{th} neutron energy regime. The gaussian width parameter after variable transformation in Equation (14), $\left(\frac{\sigma_{\mathrm{i}} z}{d_{\mathrm{iso}}}\right)$ scales with depth z to take into account geometric magnification.

Finally, $\phi_{\mathrm{i}}(E_{\mathrm{n}})$, represents the contribution of spectral fluence to a point in the phantom from i^{th} neutron regime, where $\phi_1(E_{\mathrm{n}})$ denotes the contribution from thermal neutrons, $\phi_2(E_{\mathrm{n}})$ denotes the contribution from $1/E_{\mathrm{n}}$ neutrons, $\phi_3(E_{\mathrm{n}})$ denotes the contribution from evaporation neutrons, and $\phi_4(E_{\mathrm{n}})$ denotes the contributions from high-energy neutrons.

Thermal neutrons follow a Maxwellian distribution in energy, or

$$\phi_1(E_\mathrm{n}) = a \;\; E_\mathrm{n} \;\; e^{\frac{-E_\mathrm{n}}{K_\mathrm{B}T}} \tag{15}$$

where a is the magnitude, K_B is Boltzmann constant, and $K_\mathrm{B}T$ is the most probable kinetic energy, which is equal to 0.025 eV, corresponding to absolute temperature T of 293 K.

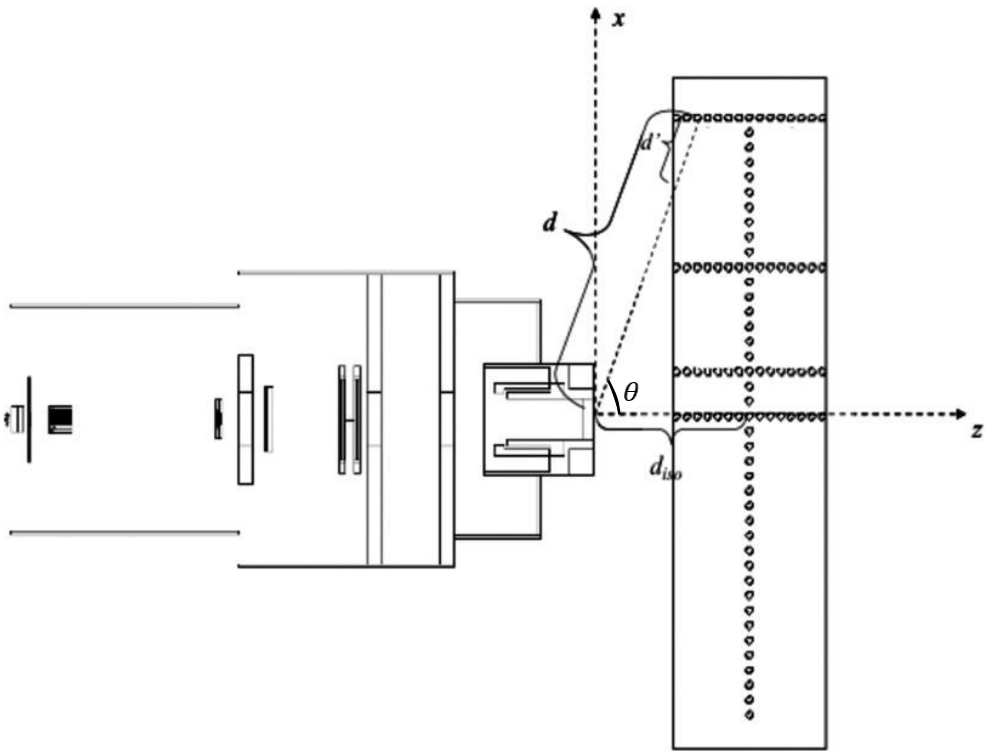

Figure 2.2. Geometry of a general-purpose proton treatment head and water phantom. Adapted from Perez-Andujar et al. (2013).

The distribution of $1/E_\mathrm{n}$ neutrons in energy was modeled as

$$\phi_2(E_\mathrm{n}) = \frac{b}{E_\mathrm{n}} \;\; \mathrm{cnorm}\left(E_\mathrm{n}, \mu_{2,}\sigma_2{}'\right) \;\; \left[1 - \mathrm{cnorm}\left(E_\mathrm{n}, \mu_{3,}\sigma_3{}'\right)\right] \tag{16}$$

where b represents the magnitude and the cumulative normal functions restrict contributions to the epithermal energy interval, with smooth transitions to neighboring regimes. The parameters

for cumulative normal functions restrict $^1/_{E_\mathrm{n}}$ neutron contribution to other energy regimes, specifically below 10^{-7} MeV and above 1 MeV. These parameters were empirically obtained.

Evaporation neutrons were modeled using a normalized gaussian, or

$$\phi_3(E_\mathrm{n}) = \frac{c}{\sqrt{2\pi}s} \quad e^{-\left[\frac{(E_\mathrm{n}-\bar{E}_3)^2}{2s^2}\right]} \tag{17}$$

where c is the magnitude, $\bar{E}_3$ is the mean energy of evaporation peak and s is the peak width parameter. Equation (15), (16) and (17) represent isotropic emission as discussed earlier.

The cascade neutrons were modeled empirically using three gaussian peaks according to

$$\phi_4(E_\mathrm{n}) = \frac{\delta}{\sqrt{2\pi}q} \quad e^{-\left[\frac{\left(E_\mathrm{n}-\bar{E}_{4,\mathrm{low}}\right)^2}{2q^2}\right]} + \frac{e}{\sqrt{2\pi}w} \quad e^{-\left[\frac{\left(E_\mathrm{n}-\bar{E}_{4,\mathrm{med}}\right)^2}{2w^2}\right]} + \frac{f(\theta)}{\sqrt{2\pi}r} \quad e^{-\left[\frac{\left(E_\mathrm{n}-\bar{E}_{4,\mathrm{high}}(E_\mathrm{p})\right)^2}{2r^2}\right]} \tag{18}$$

where δ, e, and $f(\theta)$ are peak magnitudes, q, w, and r denote the peak widths and $\bar{E}_{4,\mathrm{low}}$, $\bar{E}_{4,\mathrm{mid}}$, and $\bar{E}_{4,\mathrm{high}}(E_\mathrm{p})$ are the mean energies, respectively. Physically the peaks correspond to neutrons generated through proton and single nucleon interactions, proton and multiple nucleon interactions and pre-equilibrium emission.

The mean energy of the highest energy gaussian of the cascade neutron regime, $\bar{E}_{4,\mathrm{high}}(E_\mathrm{p})$, has linear dependence on incident proton energy, as was expected from considerations of relativistic head on collision of nucleons, or

$$\bar{E}_{4,\mathrm{high}}(E_\mathrm{p}) = \alpha_\mathrm{p} E_\mathrm{p} - \beta_\mathrm{p} \tag{19}$$

where α_p and β_p are empirical fit parameters. Similarly, $\bar{E}_{4,\mathrm{med}}$ was proportional to $\bar{E}_{4,\mathrm{high}}(E_\mathrm{p})$

$$\bar{E}_{4,\mathrm{med}} = \gamma\, \bar{E}_{4,\mathrm{high}}(E_{\mathrm{p}}) \tag{20}$$

where γ is empirical fit parameter. All of the neutrons in the "cascade regime" were modeled with isotropic emission, except those from nucleon-nucleon collisions (*i.e.*, the last term in Equation (18)), which takes into account the directional dependence of emission of the highest energy neutrons that are preferentially emitted in the forward cone, or

$$f(\theta) = \alpha_{\mathrm{f}} - \beta_{\mathrm{f}}\, \theta \tag{21}$$

where θ is the angle between the central axis and a ray from the source to the calculation point $p(x, y, z)$ (Figure 2.2), and α_{f} and β_{f} are empirical fit parameters.

2.3.2 Neutron Spectral Fluence Data

We used neutron spectral fluence and energy deposition data from simulations of the passive scattering system (Perez-Andujar et al. 2013). These simulations used the Monte Carlo Proton Radiotherapy Treatment Planning (MCPRTP) system (Newhauser et al. 2007), which leverages the Monte Carlo N-Particle eXtended (MCNPX) Radiation Transport Code (Hendricks et al. 2006). MCNPX is commonly used for simulating neutron exposures and previously has been extensively benchmarked against measurements (Tayama et al. 2002, Fontenot et al. 2005, Herault et al. 2005, Tayama et al. 2006, Koch et al. 2008, Farah et al. 2014). Simulations were performed for an 18×18 cm^2 field prior to the final collimator, which was fully closed. Neutron absorbed dose and neutron spectral fluence were tallied in simulations of pristine proton beams with mean energies at the nozzle entrance of 100, 120, 140, 160, 180, 200, 225, and 250 MeV. Neutron spectral fluence was tallied in equally spaced logarithmic neutron energy bins (40 bins per decade). A water phantom of size $30 \times 180 \times 44$ cm^3 was used with 100 spherical tally volumes, each 1cm in diameter. The tally volumes were located along the lines parallel to the

beam axis at 0 cm, 12 cm, 40 cm, and 80 cm off-axis, as well as one-line perpendicular to the beam axis at the depth of isocenter in the phantom (22 cm) (see Figure 2.2).

2.3.3 Training of Analytical Model of Neutron Spectral Fluence

We trained our neutron spectral fluence model for the general-purpose beamline at MDACC, using data from all the tally volumes (Figure 2.2) with proton beam energies of 120 MeV, 140 MeV, 160 MeV, 180 MeV, 200 MeV, 225 MeV and 250 MeV. The 100-MeV spectral fluence data was not available. The spectral fluence model was fit simultaneously to all 672 simulated neutron spectra using the Marquardt-Levenberg algorithm of (GNUPLOT Version 5.2) (Williams et al. (2017)) and minimizing weighted sum squared error (WSSR) until a preset criterion (10^{-5}, which was the default value) was met. Simultaneously fitting all spectra allowed direct and global estimation of all fitting parameters, including parameters that have no explicit dependence on proton energy or position in the phantom. All of the empirical fitting parameters were selected by minimizing the local relative differences in spectral fluence. The fitting process took into account the statistical uncertainties in the spectral fluence from Monte Carlo simulations via WSSR. Additionally, the mean energy of the evaporation peak, $\bar{E}_3$, and low-energy cascade peak, $\bar{E}_{4,\mathrm{low}}$, were constrained to be greater than 0.9 MeV based on measured spectra (Trinkl et al. 2017). Finally, the exponent τ of the neutron fluence-divergence factor was restricted to be less than 2, which is the maximum physically possible value corresponding to inverse-square divergence from a point source of radiation.

2.3.4 Model Validation

To validate the neutron spectral fluence model (Eq. (10)) we used three separate approaches. First, we integrated it according to

$$\Phi = \int_0^{E_{\max}} \phi(E_{\mathrm{n}})\ \mathrm{d}E_{\mathrm{n}} = \sum_{\mathrm{j}} \phi_{\mathrm{j}}(E_{\mathrm{n}})\ \Delta E_{\mathrm{j}} \tag{22}$$

where $\phi_{\mathrm{j}}(E_{\mathrm{n}})$ is the differential fluence in the j^{th} bin of the neutron spectral fluence and ΔE_{j} is the width of that bin.

In the second approach, we compared values of the neutron-fluence-weighted mean neutron energy, $\bar{E}_{\mathrm{n}}$, from MC simulations and analytical model calculations. The mean was calculated using

$$\bar{E}_{\mathrm{n}} = \frac{\int_0^{E_{\max}} \phi(E_{\mathrm{n}})\ E_{\mathrm{n}}\ dE_{\mathrm{n}}}{\int_0^{E_{\max}} \phi(E_{\mathrm{n}})\ \mathrm{d}E_{\mathrm{n}}} = \frac{\sum_{\mathrm{j}} \phi_{\mathrm{j}}(E_{\mathrm{n}})\, E_{\mathrm{n}}\, \Delta E_{\mathrm{j}}}{\sum_{\mathrm{j}} \phi_{\mathrm{j}}(E_{\mathrm{n}})\ \Delta E_{\mathrm{j}}} \tag{23}$$

where $\phi_{\mathrm{j}}(E_{\mathrm{n}})$ is the differential fluence in the j^{th} bin of the neutron spectral fluence and ΔE_{j} is the width of that neutron energy bin.

In the third approach we calculated the neutron-fluence-weighted mean neutron kerma coefficient as

$$\bar{k}_{\phi}(E_{\mathrm{n}}) = \frac{\int_0^{E_{\max}} \phi(E_{\mathrm{n}})\ k_{\phi}(E_{\mathrm{n}})\, \mathrm{d}E_{\mathrm{n}}}{\int_0^{E_{\max}} \phi(E_{\mathrm{n}})\ \mathrm{d}E_{\mathrm{n}}} = \frac{\sum_{\mathrm{j}} \phi_{\mathrm{j}}(E_{\mathrm{n}})\ k_{\phi}(E_{\mathrm{n}})\, \Delta E_{\mathrm{j}}}{\sum_{\mathrm{j}} \phi_{\mathrm{j}}(E_{\mathrm{n}})\ \Delta E_{\mathrm{j}}} \tag{24}$$

where $\phi_{\mathrm{j}}(E_{\mathrm{n}})$ is the differential fluence in the j^{th} bin of the neutron spectral fluence and ΔE_{j} is the width of that energy bin. To cross check the calculation of $\bar{k}_{\phi}(E_{\mathrm{n}})$ in Equation (24), we also calculated it as

$$\bar{k}_{\phi}(E_{\mathrm{n}}) = k_{\phi}(\bar{E}_{\mathrm{n}}) \tag{25}$$

where $\bar{E}_{\mathrm{n}}$ was taken from Equation (23).

2.4 Kerma Calculation

Using the kerma coefficient model and neutron spectral fluence model, kerma at a point was calculated using Equation (5). To cross check this result, we calculated kerma as

$$K = \Phi \; k_{\phi}(\overline{E}_{\mathrm{n}}) \tag{26}$$

where Φ is the fluence from Equation (22).

2.5 Absorbed-Dose Calculation

2.5.1 Kerma-to-Absorbed-Dose Conversion Factor

Kerma and absorbed dose are two different physical quantities that are related but not numerically equal, except where CPE exists. Thus, in general a conversion factor, $F_{K\to D}$, is needed to transform kerma to absorbed dose. This conversion factor is given by

$$D_{\mathrm{MC}} = F_{K\to D} \; K_{\mathrm{MC}}$$

$$F_{K\to D} = \frac{D_{\mathrm{MC}}}{K_{\mathrm{MC}}}$$

$$= \frac{D_{\mathrm{MC}}}{\int_0^{E\max} \phi(E_{\mathrm{n}}) \; k_{\phi}^{\mathrm{MC}}(E_{\mathrm{n}}) \, \mathrm{d}E_{\mathrm{n}}}$$

$$= \frac{D_{\mathrm{MC}}}{\int_0^{E_{\max}} \phi(E_{\mathrm{n}}) \; k_{\phi}^{\mathrm{ICRU}}(E_{\mathrm{n}}) \, \mathrm{d}E_{\mathrm{n}}} \times \frac{\int_0^{E_{\max}} \phi(E_{\mathrm{n}}) \; k_{\phi}^{\mathrm{ICRU}}(E_{\mathrm{n}}) \, \mathrm{d}E_{\mathrm{n}}}{\int_0^{E_{\max}} \phi(E_{\mathrm{n}}) \; k_{\phi}^{\mathrm{MC}}(E_{\mathrm{n}}) \, \mathrm{d}E_{\mathrm{n}}} \tag{27}$$

If we assume equivalence of $k_{\phi}^{\mathrm{ICRU}}(E_{\mathrm{n}})$ and $k_{\phi}^{\mathrm{MC}}(E_{\mathrm{n}})$, the second term in equation becomes equal to 1, yielding

$$F_{K\to D} = \frac{D_{\mathrm{MC}}}{\int_0^{E_{\max}} \phi(E_{\mathrm{n}}) \; k_{\phi}^{\mathrm{ICRU}}(E_{\mathrm{n}}) \, \mathrm{d}E_{\mathrm{n}}} \tag{28}$$

where, D_{MC} is dose from MC simulations.

2.5.2 Surface Correction Factor

To account for interface effects near the surface of the phantom, we used an empirical shallow-depth correction factor given by,

$$F_{\mathrm{S}} = \begin{cases} \alpha_{\mathrm{s}}(1 - e^{-\mu_{\mathrm{s}} z}) & x \leq 40 \text{ cm} \\ 1 & x > 40 \text{ cm} \end{cases} \tag{29}$$

where α_{s}, μ_{s} are fit parameters, x is off axis distance and z is depth in water.

Finally, with inclusion of kerma-to-absorbed-dose conversion factor and surface-correction factor the absorbed dose is given by

$$D_{\mathrm{AM}} = F_{\mathrm{S}}\ F_{K \to D}\ K_{AM} \tag{30}$$

where K_{AM} is kerma calculated using Equation (6).

Chapter 3. Results

3.1 Empirical Model of Kerma Coefficient

Table 3.1 lists the parameters for the analytical model for neutron kerma coefficients (Eq. 9) for the materials listed in table C.3 in ICRU Report 63 (2000). The model was in excellent agreement over the energy interval from 2.53×10^{-8} MeV to 150 MeV for water with average 1.20% relative difference. Figure 3.1 shows agreement between our model and evaluated ICRU data for neutron kerma coefficients in water. Further this model was in good agreement for other materials with average relative difference within 6% as illustrated in Table 3.2.

Table 3.1. Parameters from fitting neutron kerma coefficient values to proposed analytical model [Eq. (9)].

Material	a_1 (fGy m^2)	b_1 (fGym^{2}MeV)	μ_1 (MeV)	σ_1' (MeV)	u (10^{-4}) (fGym^{2}MeV^{-2})	v (fGy m^2)
A150 Plastic	2.697×10^{-5}	59.25	3.333	1.754	2.754	7.622
Water	4.645×10^{-7}	43.30	2.705	1.571	2.377	7.402
Muscle	2.731×10^{-5}	46.49	2.911	1.627	2.491	7.140
Bone	2.112×10^{-5}	82.57	4.285	1.943	2.706	5.738
TE − Meth	2.412×10^{-5}	53.71	3.114	1.690	2.628	7.387
TE − Prop	2.395×10^{-5}	53.98	3.163	1.685	2.641	7.307

Note: All significant digits provided should be used to calculate kerma coefficient values and threshold energy, $E_{\mathrm{n,Thresh}}$, of 23 MeV was used for all materials.

Higher energy neutrons contributes the majority of kerma because of larger fluence and kerma coefficient values at higher energies. Since the ICRU tabulated data ranges from thermal energies up to 150 MeV, extrapolation was used beyond that energy as shown in Figure 3.1.

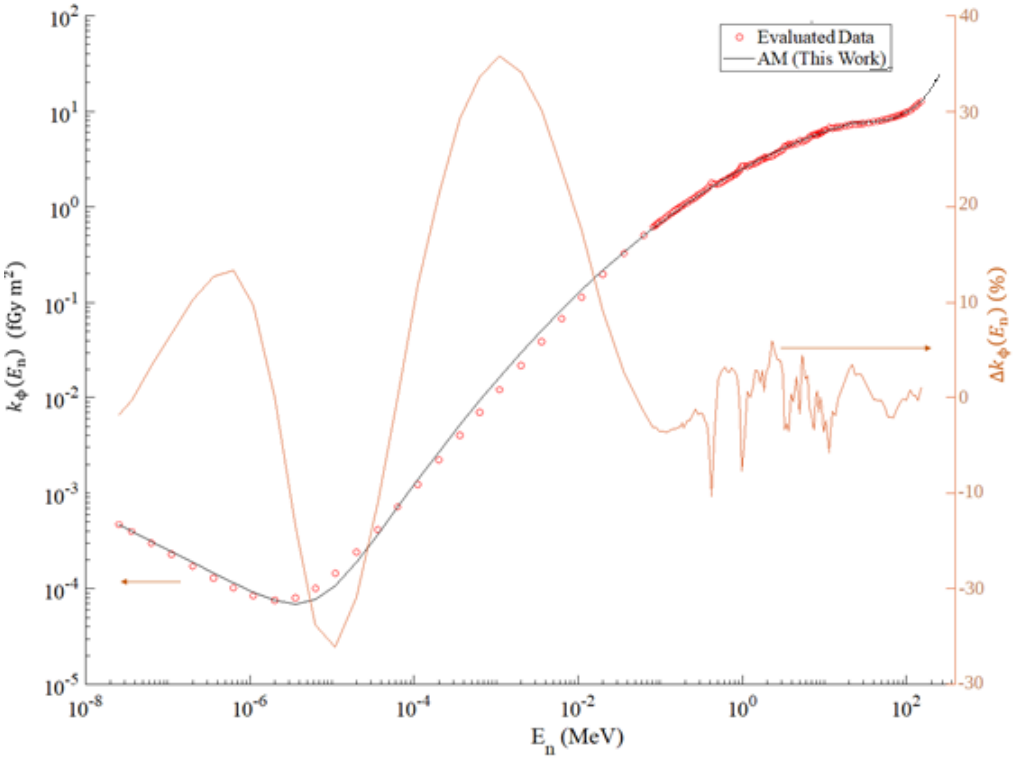

Figure 3.1. Neutron kerma coefficient $k_\phi(E_\mathrm{n})$ *versus* neutron energy, E_n, in water. Data are from ICRU Report 63 (points) and the analytical model [Eq. (9)] (line). The absolute difference between kerma coefficient, $\Delta k_\phi(E_\mathrm{n})$, are also plotted (right ordinate).

Table 3.2. Average and maximum relative difference in neutron kerma coefficients between data from ICRU Report 63 and the analytical model over energy range from 2.53×10^{-8} MeV to 150 MeV [Eq. (9)].

Material	Average Difference (%)	Maximum Difference (%)
A150 Plastic	5.110	104.32
Water	1.200	35.76
Muscle	5.110	53.42
TE – Methane	5.800	81.67
TE – Propane	3.630	84.05
Bone	2.400	93.61

3.2 Analytical Model of Neutron Spectral Fluence

3.2.1 Parameter Values

Table 3.3 lists the parameters of the analytical model that govern the $\phi_i(E_n)$ in Equations (15) to (18), AF_i in Equation (13) and OAF_i in Equation (14). The parameters governing energy scaling (Eq. 11) are in Table 3.4. These parameters were used to evaluate Equation (10) to calculate neutron spectral fluences. As expected, the effective gaussian width parameters of OAF's for the low energy neutron regimes, epithermal and thermal, are large corresponding to isotropic distribution whereas it is small for cascade neutrons because of their emission in the forward direction. The exponent, τ, governing divergence of neutron fluence was found to be 1.013. Figure 3.2 plots spectral fluence at isocenter, demonstrating how it varies with proton beam energy.

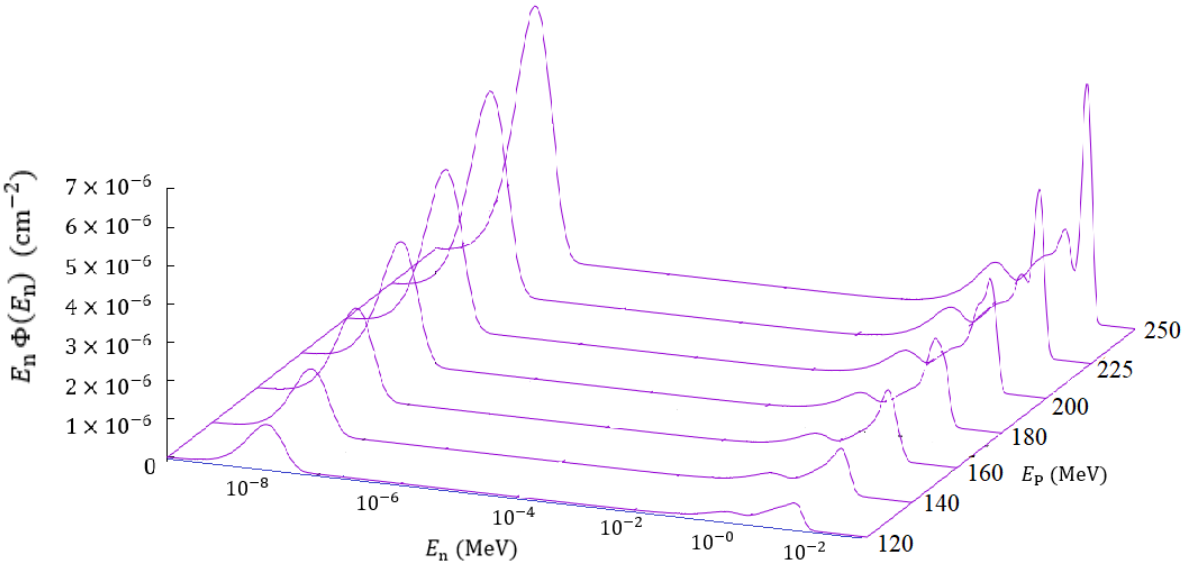

Figure 3.2. Selected examples of neutron spectral fluence at isocenter produced by 120 to 250-MeV proton beams. These were calculated using the analytical model [Eq. (10)].

Table 3.3. Parameters governing neutron spectral fluence, $\phi_i(E_n)$ [Eq. (15-18)], neutron attenuation factor, AF_i [Eq. (13)] and off-axis factor, OAF_i [Eq. (14)]

Neutron Energy Regime	Parameter	Value	Units
Thermal	a	2.04×10^{10}	$\mathrm{cm^{-2}\ MeV^{-1}}$
	α_1	0.036	$\mathrm{cm^{-1}}$
	σ_1	85.85	cm
$1/E_n$	b	1.07×10^{-7}	$\mathrm{cm^{-2}\ MeV}$
	μ_2	10^{-7}	MeV
	σ_2'	3.3×10^{-8}	MeV
	μ_3	1.0	MeV
	σ_3'	0.5	MeV
	α_2	0.033	$\mathrm{cm^{-1}}$
	σ_2	86.51	cm
Evaporation	c	1.1×10^{-7}	$\mathrm{cm^{-2}\ MeV}$
	s	2.81	MeV
	$\bar{E}_3$	0.9	MeV
	α_3	0.013	$\mathrm{cm^{-1}}$
	σ_3	16.11	cm
Cascade	d	1.88×10^{-6}	$\mathrm{cm^{-2}\ MeV}$
	e	4.71×10^{-7}	$\mathrm{cm^{-2}\ MeV}$
	$\bar{E}_{4,\mathrm{low}}$	1.01	MeV
	γ	0.78	–
	q	18.26	MeV
	w	18.78	MeV
	r	29.41	MeV
	α_f	1.67×10^{-6}	$\mathrm{cm^{-2}\ MeV}$
	β_f	1.23×10^{-8}	$\mathrm{cm^{-2}\ MeV}$
	α_p	0.93	–
	β_p	82.70	MeV
	α_4	0.013	$\mathrm{cm^{-1}}$
	σ_4	44.42	cm

Table 3.4. Parameters for modeling dependence of neutron spectral fluence on proton beam energy, as defined in Equation (11).

Parameter	Value	Units
α_E	6704.46	–
ξ	2.53	–

Figure 3.3 and 3.4 are illustrative examples of how well the analytical model reproduced neutron spectral fluence data from MC simulations.

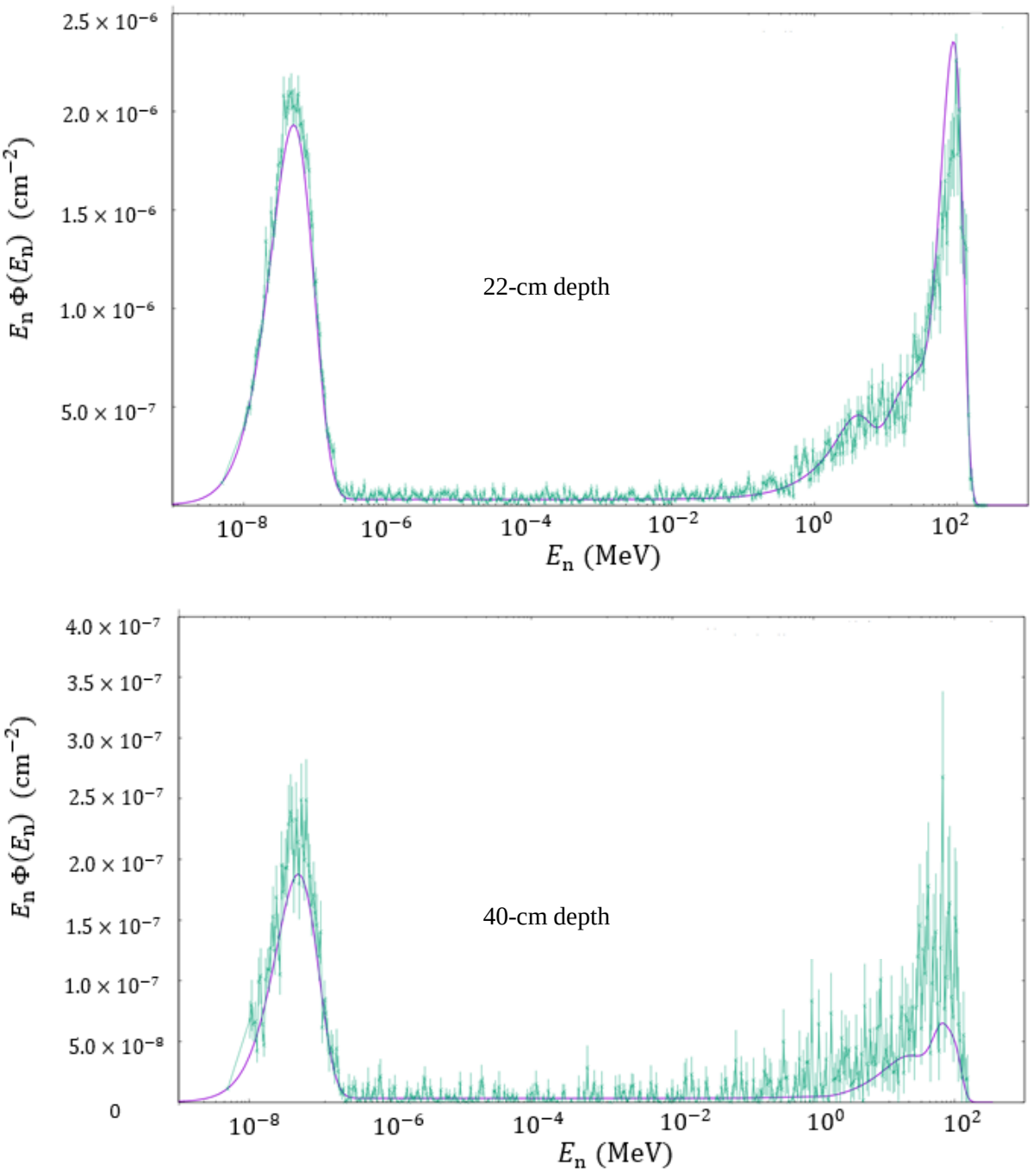

Figure 3.3. Selected examples of neutron spectral fluence at 22-cm and 40-cm water depth along central axis produced by 180-MeV proton beams. Green lines with error bars represent data from Monte Carlo simulations and purple lines are from the analytical model.

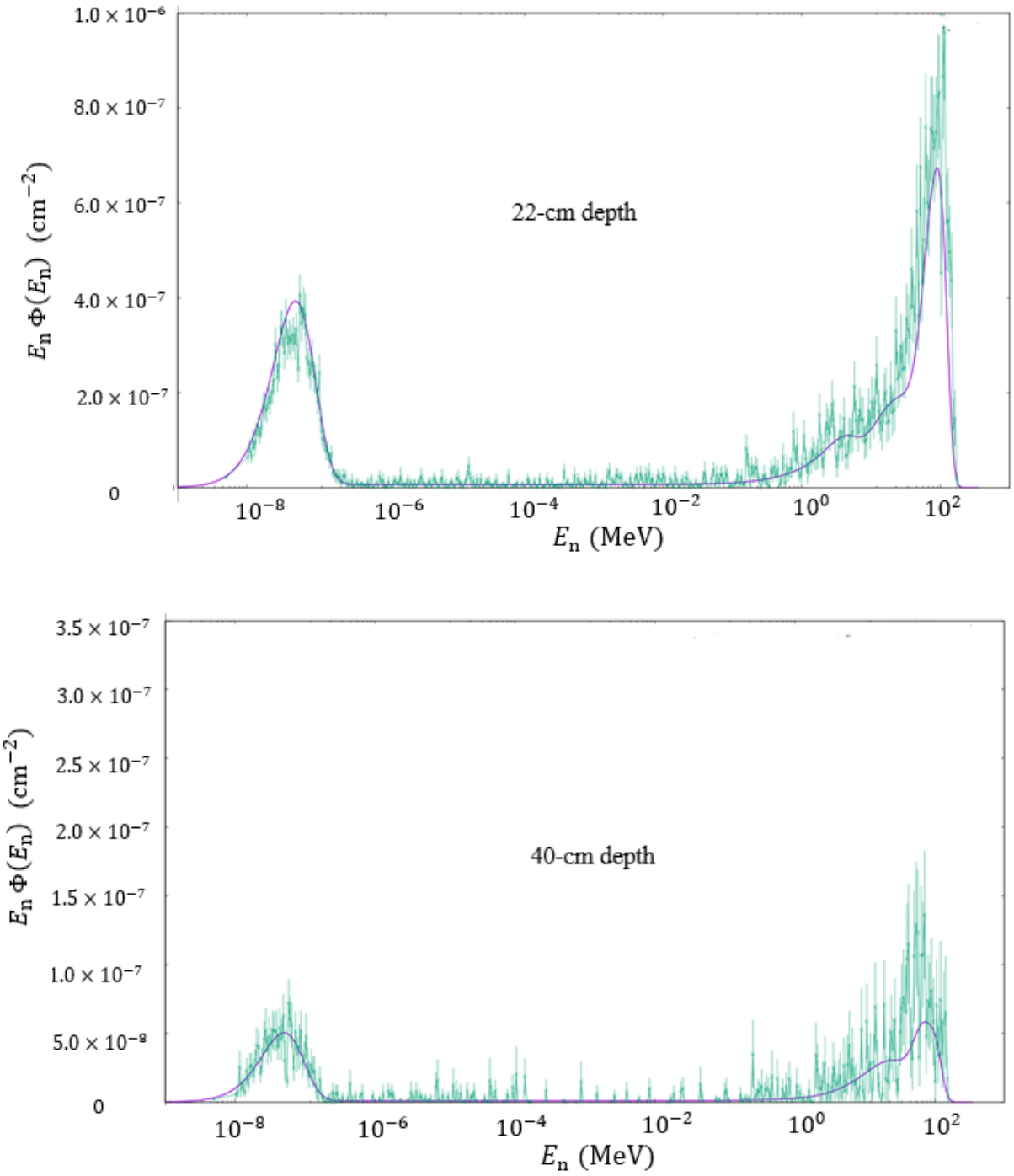

Figure 3.4. Selected examples of neutron spectral fluence at 22-cm and 40-cm water depth along 80 cm off-axis distance produced by 180-MeV proton beams. Green lines with error bars represent data from Monte Carlo simulations and purple lines are from the analytical model.

Figure 3.4 shows how well our model agrees with MC data at 22 cm (isocentric depth) and 40 cm along central axis. Figure 3.5 illustrates the agreement between analytical model and Monte Carlo data in predicting kerma contribution. As expected, kerma is predominated by from high energy cascade neutrons.

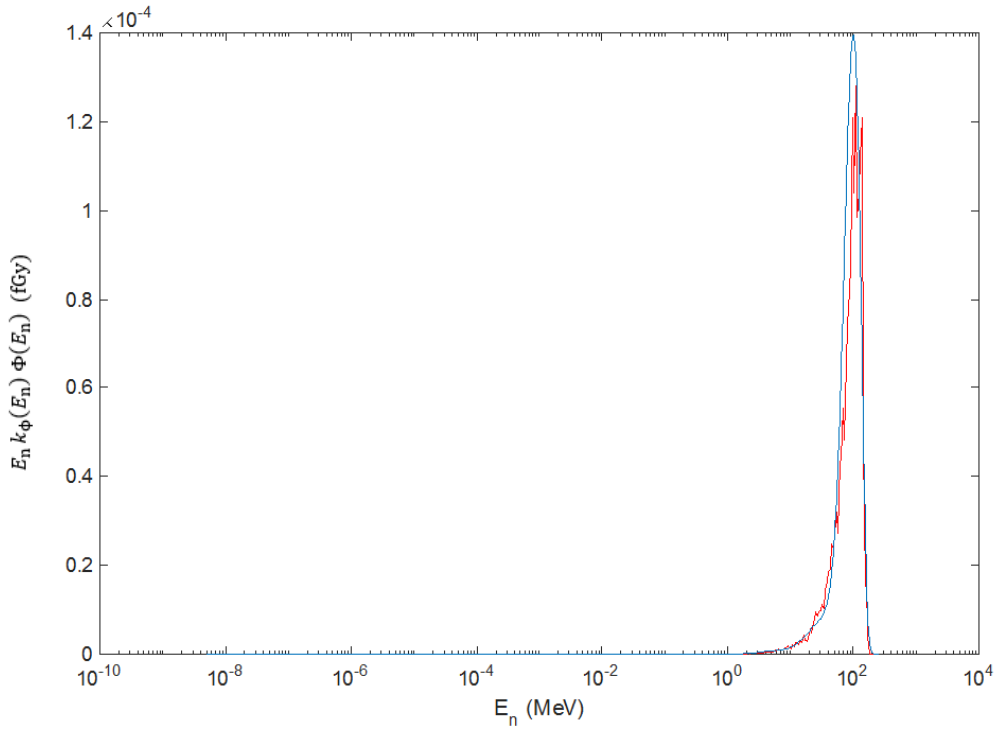

Figure 3.5. Predication of kerma contribution from Monte Carlo (red) and analytical model (blue) *versus* neutron energy at 25-cm water depth along central axis for 180-MeV proton beam.

3.2.1 Comparison of Neutron Fluence from Monte Carlo Simulation and Analytical Model

Figure 3.6 plots predictions of fluence from Monte Carlo and analytical models for 120-MeV, 180-MeV and 250-MeV proton beams in water. Figure 3.6 (a) shows the fluence variation with water depth along central axis, while Figure 3.6 (b) shows the corresponding result at 12 cm off-axis distance. Both figures demonstrate generally good agreement beyond approximately 7-cm water depth. Figure 3.7 plots lateral distribution of fluence at 22-cm water depth.

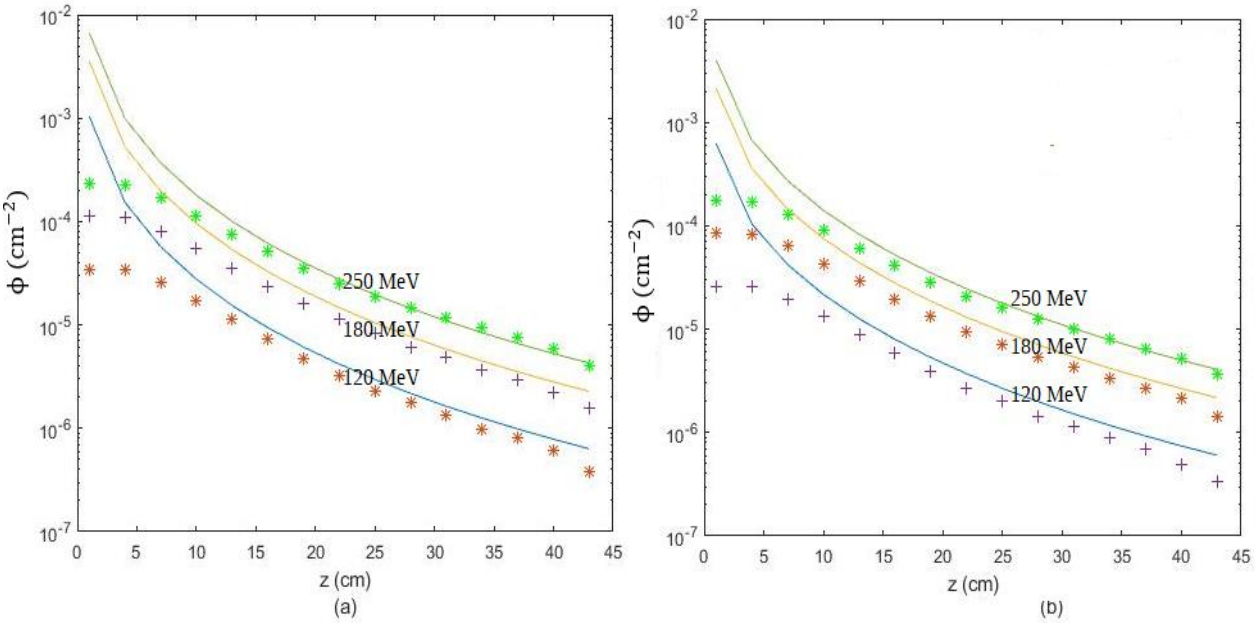

Figure 3.6. Selected example predictions from Monte Carlo (points) and analytical model (lines) of neutron fluence Φ *versus* depth z in water at (a) central axis, (b) 12-cm off-axis distance for 120-MeV, 180-MeV and 250-MeV proton beams.

.

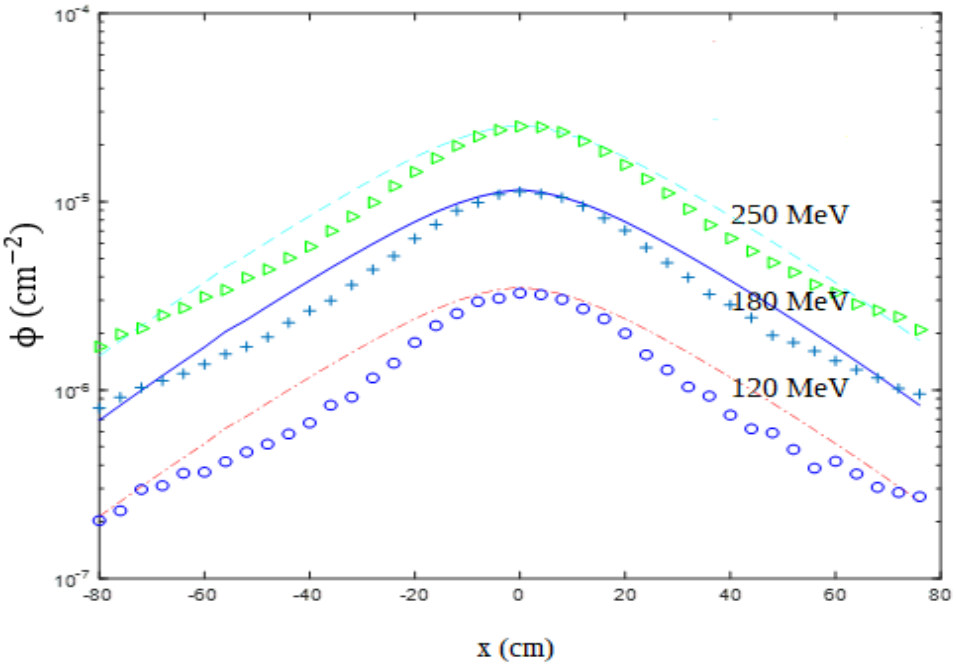

Figure 3.7. Selected example predictions from Monte Carlo (points) and analytical model (lines) of neutron fluence *versus* off-axis position at 22-cm depth in water for 120-MeV, 180-MeV and 250-MeV proton beams.

Since our analytical model of neutron spectral fluence doesn't account the loss of neutrons from the surface of the water phantom, we observed the largest disagreement at shallow depths, close to the surface, where we overestimated the fluence. The analytical model prediction of fluence is in reasonable agreement with MC data along the profile at 22 cm depth. The largest differences were observed at 40-cm off-axis distance in this case.

3.2.3 Fluence-Weighted Average Neutron Energy and Average Neutron Kerma Coefficient

Table 3.5 lists the neutron fluence-weighted average energy and neutron fluence-weighted average kerma coefficient values for selected locations for a 180-MeV proton beam, including relative differences. There is relatively good agreement between MC calculated values and analytical model except at shallower depths and far off-axis locations. The agreement was observed to improve with depth.

Table 3.5. Fluence-weighted average neutron energy, $\bar{E}_{\mathrm{n}}$, [Eq. (23)] and fluence-weighted average kerma coefficient, $\bar{k}_{\phi}$, [Eq. (24)] including relative difference for 180-MeV proton beams from analytical model (AM) calculations and Monte Carlo simulations (MC) at selected locations in a water phantom.

Location *(x, y, z)* (cm, cm, cm)	$\bar{E}_{\mathrm{n}}$			$\bar{k}_{\phi}$		
	AM (MeV)	MC (MeV)	$\frac{\mathrm{AM}-\mathrm{MC}}{\mathrm{MC}}$ (%)	AM (fGy m^2)	MC (fGy m^2)	$\frac{\mathrm{AM}-\mathrm{MC}}{\mathrm{MC}}$ (%)
(0,0,13)	9.68	7.97	21.45	1.62	1.50	8.00
(0,0,22)	21.43	18.81	13.92	3.22	2.94	9.52
(0,0,43)	38.73	46.15	−16.07	5.54	6.31	−12.20
(12,0,13)	8.38	6.77	23.78	1.34	1.38	−2.89
(12,0,22)	18.74	17.25	8.63	2.83	2.80	1.07
(12,0,43)	34.16	44.53	−23.28	4.95	6.19	−20.03
(40,0,13)	8.13	4.65	74.83	1.24	1.03	20.38
(40,0,22)	21.30	14.10	51.06	3.16	2.50	26.45
(40,0,43)	36.31	42.94	−15.44	5.29	6.11	−13.42
(80,0,13)	2.49	5.7	−56.31	0.41	1.12	−63.39
(80,0,22)	20.97	16.26	28.96	3.21	2.81	14.23
(80,0,43)	40.27	36.49	10.35	5.99	5.48	9.31

Table 3.6 lists the average and maximum relative differences between the $\bar{E}_{\mathrm{n}}$ values calculated with Monte Carlo simulations and those predicted by the analytical model. Consistent with our findings from fluence calculations, the largest differences are associated with tallies at shallow water depths and large off-axis distance.

Figure 3.8 plots the variation of fluence-weighted mean neutron energy with off-axis distance and depth for 120-MeV, 180-MeV, and 250-MeV proton beams. Average neutron energy increases with depth and reaches a maximum value and then decreases gradually. The average neutron energy decreases gradually with off axis distance and then increases. Further, average neutron energy also increases monotonically with incident proton energy.

Table 3.6. Average relative difference, $\overline{\Delta\bar{E}_{\mathrm{n}}}$, and maximum relative difference, $\Delta\bar{E}_{\mathrm{n}}\,|_{\mathrm{Max}}$, between $\bar{E}_{\mathrm{n}}$ values calculated by Monte Carlo method and analytical model [Eq. (23)].

E_{p} (MeV)	$\overline{\Delta\bar{E}_{\mathrm{n}}}$ (%)	$\Delta\bar{E}_{\mathrm{n}}\,\vert_{\mathrm{Max}}$ (%)	Location of $\Delta\bar{E}_{\mathrm{n}}\,\vert_{\mathrm{Max}}$
250	16	−99	(80,0,1)
225	19	−98	(80,0,1)
200	20	−99	(80,0,1)
180	21	−94	(80,0,1)
160	23	−99	(80,0,1)
140	23	−99	(80,0,1)
120	18	−160	(80,0,43)

Table 3.7 lists the average and maximum relative differences between the $\bar{k}_{\phi}$ values calculated with Monte Carlo simulations and the analytical model for all the energies considered. Consistent with our findings from fluence calculations and average energy comparison, the largest differences were observed at shallow water depths and at large off-axis distance.

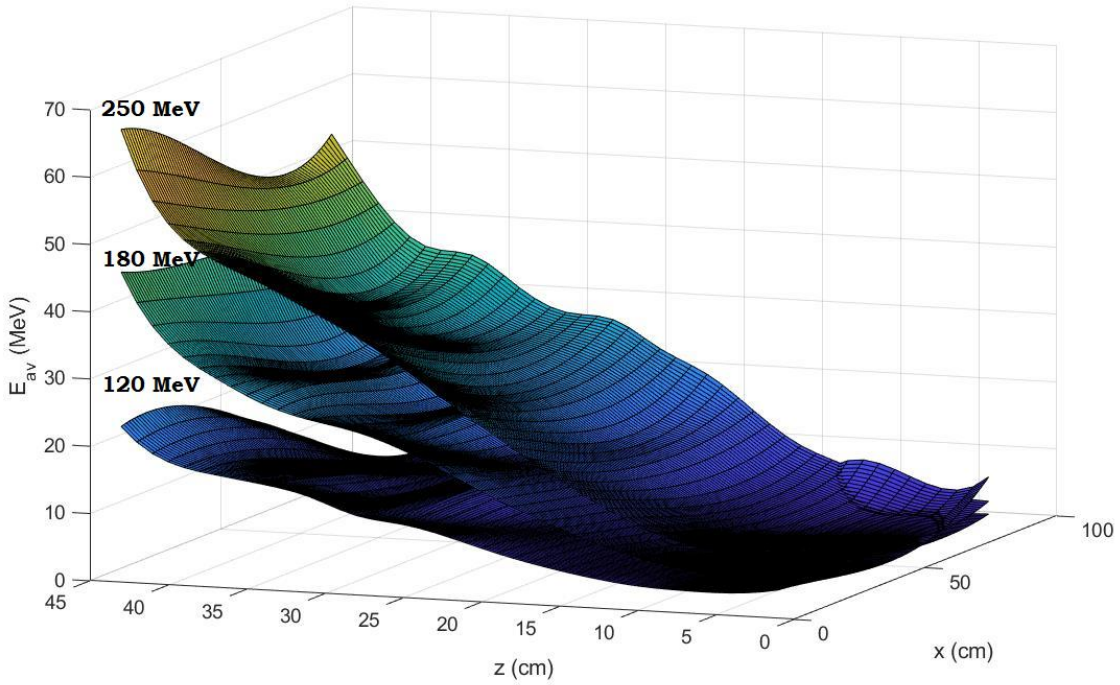

Figure 3.8. Variation of average neutron energy with off-axis distance and depth for 120-MeV, 180-MeV and 250-Mev proton beam.

Table 3.7. Average relative difference, $\overline{\Delta\bar{k}_{\phi}}$, and maximum relative difference, $\Delta\bar{k}_{\phi}|_{\mathrm{Max}}$, between $\bar{k}_{\phi}$ values calculated by Monte Carlo method [Eq. (24)] and analytical model [Eq. (25)].

E_{p} (MeV)	$\overline{\Delta\bar{k}_{\phi}}$ (%)	$\Delta\bar{k}_{\phi}\,\vert_{\mathrm{Max}}$ (%)	Location of $\Delta\bar{k}_{\phi}\,\vert_{\mathrm{Max}}$
250	29	−150	(80,0,1)
225	29	−98	(80,0,1)
200	28	−97	(80,0,1)
180	25	98	(80,0,1)
160	15	97	(80,0,1)
140	19	98	(80,0,1)
120	11	−150	(80,0,43)

3.3 Neutron Kerma Calculation

Table 3.8 lists the neutron kerma values calculated at select locations using both MC data [Eq. (26)] and the analytical model [Eq. (5)] for 120-MeV and 250-MeV proton beams. These

exhibit reasonably good agreement except at shallow depths and large off-axis distance. Figure 3.9 plots the variation of kerma calculated based on Monte Carlo simulation and our analytical model at 22-cm water depth for 120-MeV, 180-MeV and 250-MeV proton beams. Consistent with previous results we see that our model predicts kerma with relatively good accuracy near the central axis but overpredicts the fluence at 40-cm off-axis distance.

Table 3.8. Select examples of neutron kerma and relative difference for 120-MeV and 250-MeV proton beams from analytical model (AM) [Eq. (5)] and Monte Carlo simulations (MC) using [Eq. (26)].

Location *(x,y,z)* (cm, cm, cm)	$E_p = 250$ MeV			$E_p = 120$ MeV		
	K_{AM} (Gy)	K_{MC} (Gy)	Diff (%)	K_{AM} (Gy)	K_{MC} (Gy)	Diff (%)
(0,0,22)	9.37×10^{-16}	9.22×10^{-16}	1.6	8.15×10^{-17}	7.34×10^{-17}	11
(12,0,22)	8.77×10^{-16}	7.30×10^{-16}	20	7.37×10^{-17}	5.71×10^{-17}	29
(40,0,22)	5.35×10^{-16}	2.11×10^{-16}	128	3.85×10^{-17}	1.27×10^{-17}	203
(80,0,22)	1.15×10^{-16}	6.09×10^{-17}	69	8.35×10^{-18}	4.11×10^{-18}	103

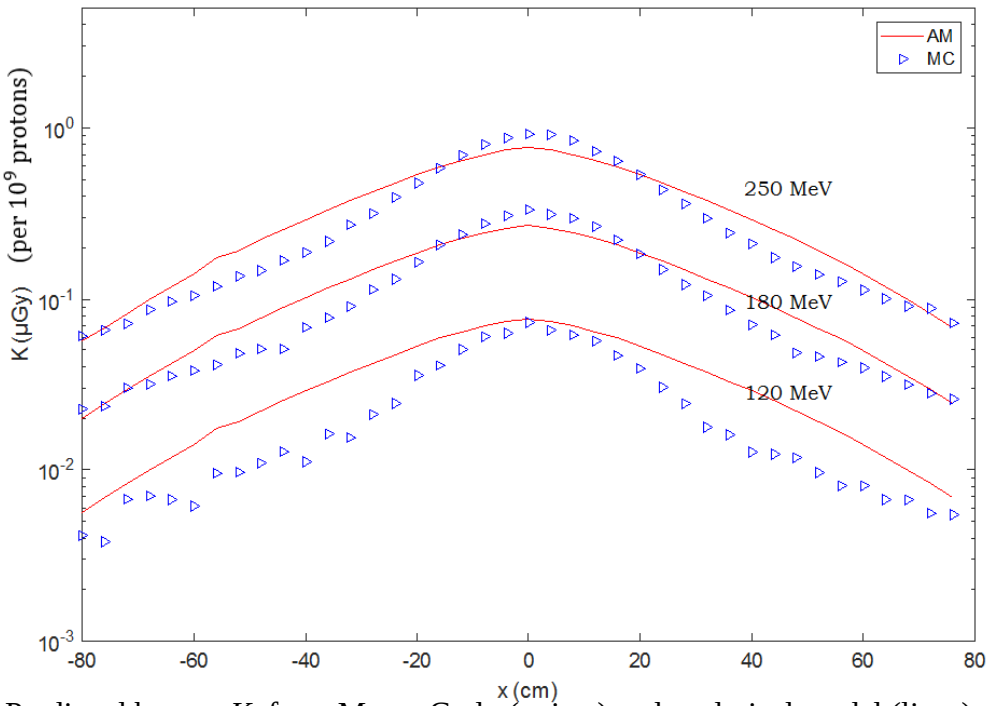

Figure 3.9. Predicted kerma, *K*, from Monte Carlo (points) and analytical model (lines) of kerma *versus* off-axis position, *x*, at 22-cm depth in a water for 120-MeV, 180-MeV and 250-MeV proton beam.

3.4 Absorbed-Dose Calculation

3.4.1 Kerma-to-Absorbed Dose Conversion Factor and Surface Correction Factor

Using Eq. (28), we calculated kerma-to-absorbed-dose conversion factor, $F_{K\to D}$ at all the tally locations. Figure 3.10 plots variation of absorbed dose reported by MC and kerma calculated using MC data for 180-MeV proton beam with off-axis distance whereas Figure 3.11 plots $F_{K\to D}$ versus off-axis distance for the same case. Absorbed dose along the profile was found to be slightly greater than kerma for most locations. The fluctuations in kerma-to-absorbed-dose conversion factors were averaged and a value of 1.18 was used as conversion factor.

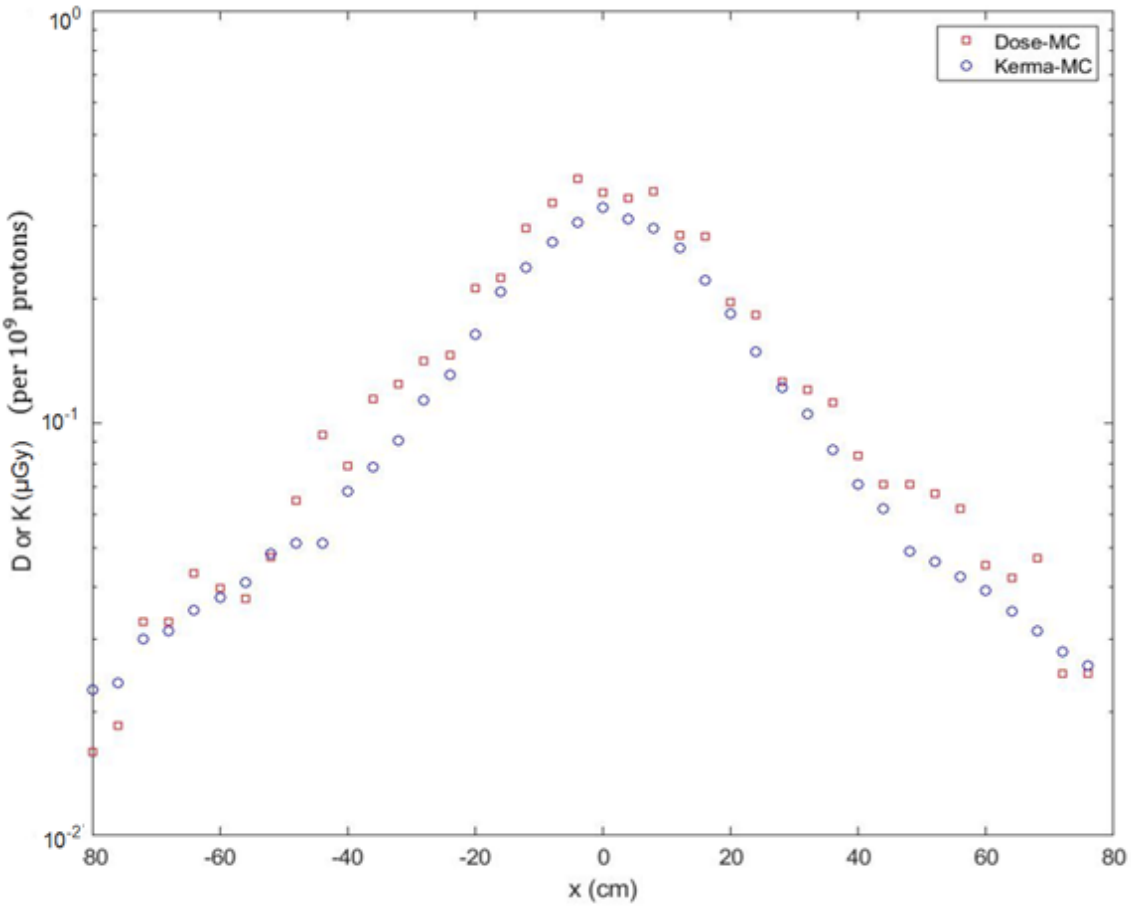

Figure 3.10. Comparison of absorbed-dose, *D*, and kerma, *K*, calculated using MC data *versus* off-axis distance xfrom a 180-MeV proton beam at 22-cm depth in a water phantom.

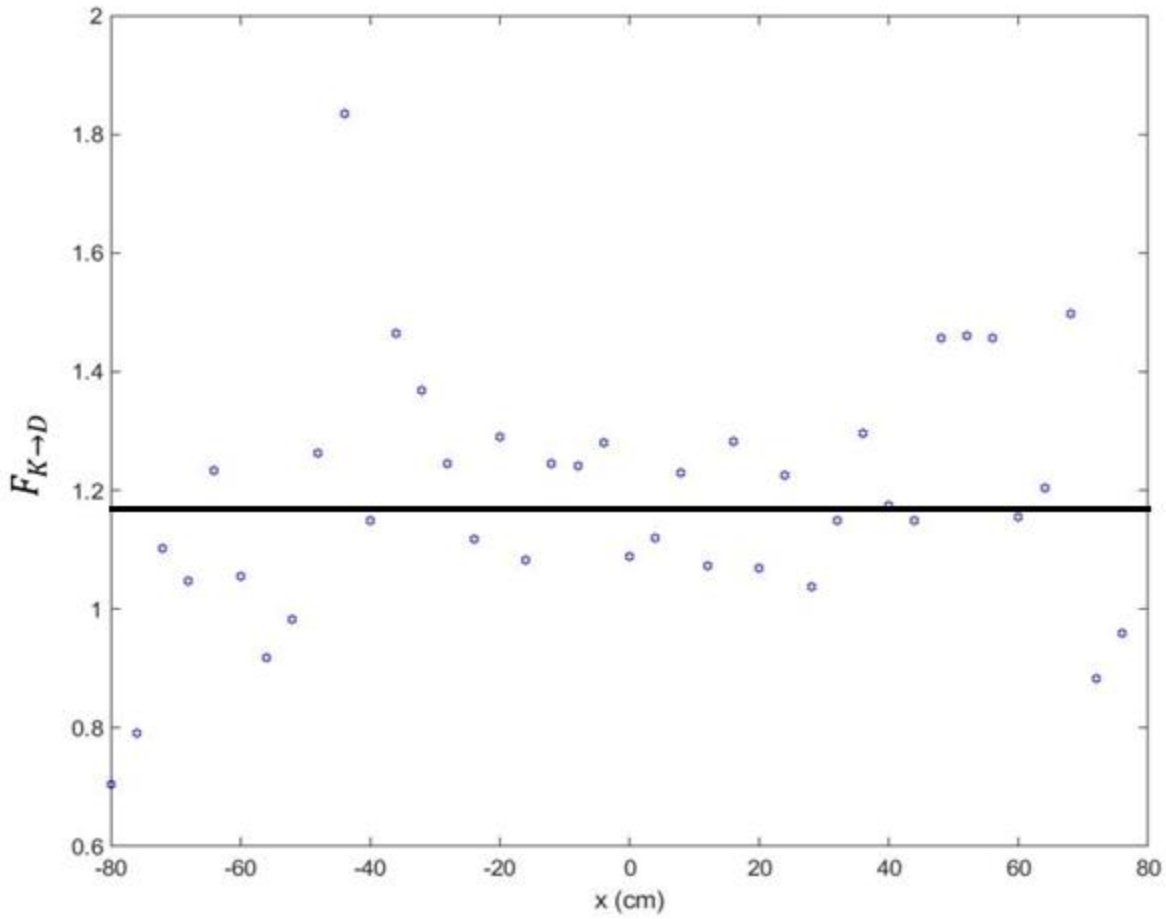

Figure 3.11. Kerma-to-absorbed dose conversion factor, $F_{K\to D}$, *versus* off-axis distance for 180-MeV proton beam at 22-cm depth.

The values of the parameters governing the shallow depth correction (Eq. 29) α_s and $\mu_s$were empirically found to be 0.72 and 0.2781 cm^{-1} respectively.

3.4.2 Corrected Absorbed Dose Calculation

We utilized the kerma-to-absorbed-dose conversion factor and surface correction factor to calculate absorbed dose in water using Equation (30). The absorbed dose from MC simulation and our model are shown in Figure 3.12, revealing relatively good agreement. Consistent with our fluence and kerma predictions, our model predicts dose with relatively good accuracy along central axis and a slight overprediction of absorbed dose near 40 cm off-axis distance.

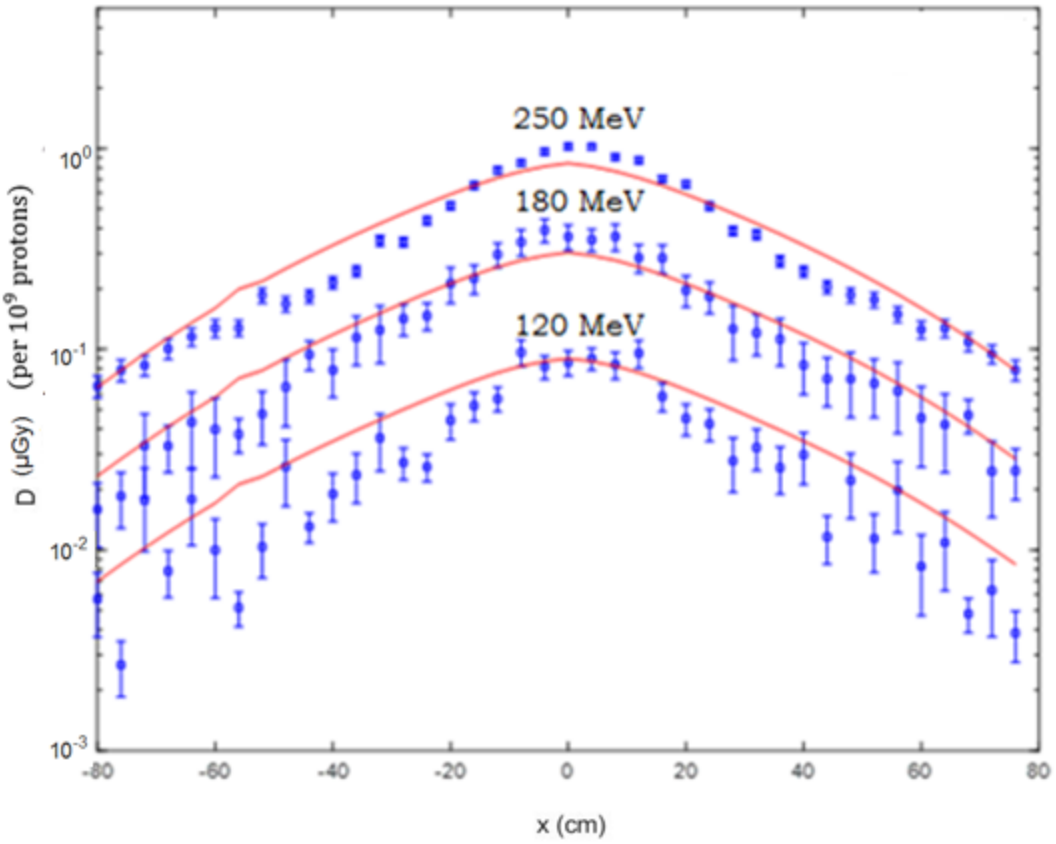

Figure 3.12. Predictions of absorbed dose, *D*, from analytical model (lines) and Monte Carlo calculation (points) *versus* off-axis distance, *x*, in water for 120-MeV, 180-MeV and 250-MeV proton beams at 22-cm depth.

Figure 3.13 plots the absorbed dose *versus* depth along central axis from the MC simulations and analytical model for 120-MeV, 180-MeV and 250-MeV proton beams. The figure reveals good agreement between the MC and analytical model predictions. Table 3.9 lists the average relative difference, $\Delta\overline{D}$, and the maximum relative difference, $\Delta\overline{D}\,|_{\mathrm{Max}}$, between values. The average relative difference at all the locations in phantom for all energies was about 50%. The maximum relative differences were observed mostly at 80-cm off-axis distances and at deeper depths where our model overestimates absorbed dose.

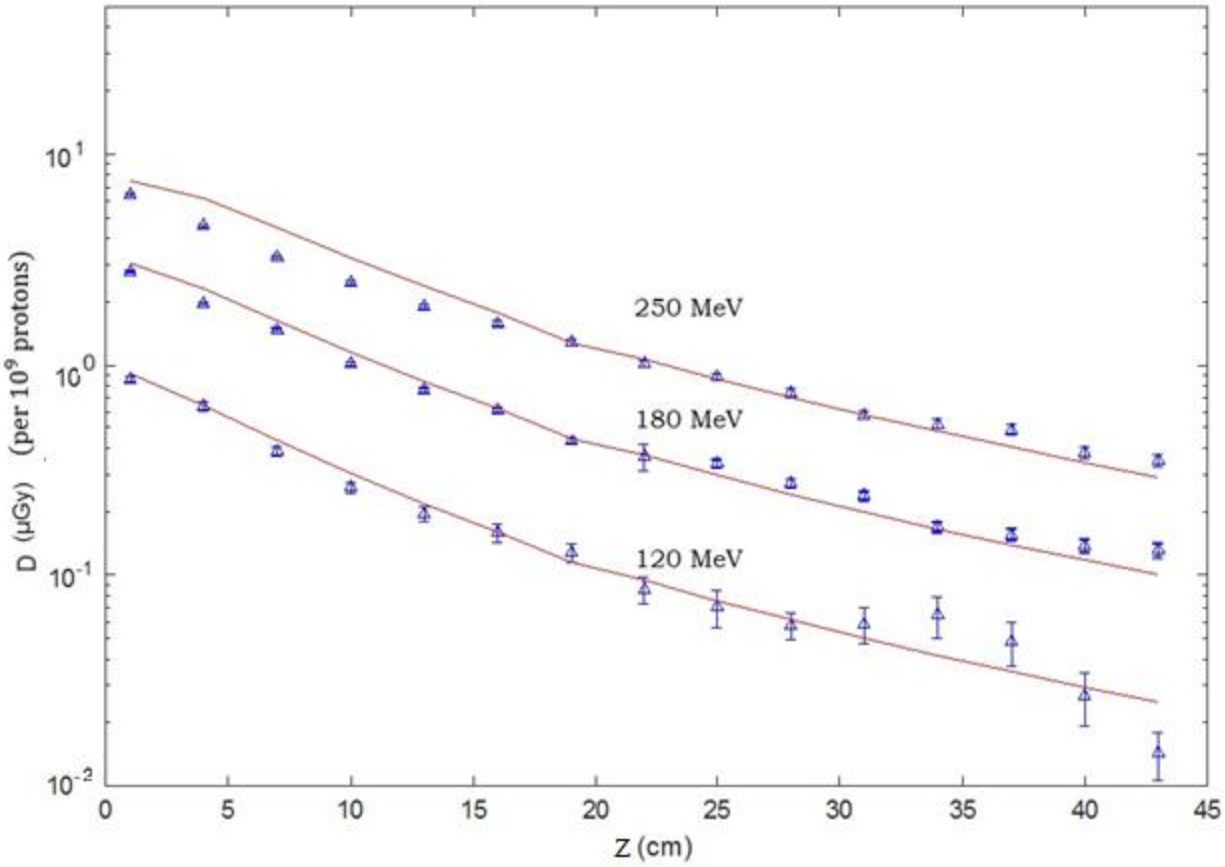

Figure 3.13. Prediction of absorbed dose, *D*, from analytical model (lines) and Monte Carlo calculation (points) *versus* depth in water, *z*, for 120-MeV, 180-MeV and 250-MeV proton beams.

Table 3.9. Average relative difference, $\overline{\Delta D}$, and maximum relative difference, $\Delta D\,|_{\mathrm{Max}}$, between absorbed-dose values calculated by Monte Carlo method and the analytical model considering all the tally volumes in the water phantom.

E_{p} (MeV)	$\overline{\Delta D}$ (%)	$\Delta D\,\|_{\mathrm{Max}}$ (%)	Location of $\Delta D\,\|_{\mathrm{Max}}$ (x, y, z) cm
250	52	217	(80,0,40)
225	50	173	(80,0,37)
200	43	187	(80,0,27)
180	52	269	(80,0,43)
160	47	264	(80,0,28)
140	54	263	(80,0,37)
120	92	374	(80,0,27)

Chapter 4. Discussion

An analytical model was developed to calculate the neutron spectral fluence, kerma, and absorbed dose in a water-box phantom for passively scattered proton therapy beams of 120 MeV to 250 MeV. The model calculates neutron spectral fluence, then applies neutron kerma coefficients to obtain kerma, and finally applies a kerma-to-absorbed dose conversion factor and a surface correction factor. Evidently, it is possible to predict absorbed dose due to stray neutrons with an analytical approach within reasonable accuracy. Average relative difference observed in case of neutron spectral fluence, neutron kerma coefficient and absorbed dose were approximately 23%, 6% and 50% respectively.

This model, with some refinements, appears potentially suitable for integration in treatment planning system. Because the model is physics-based, we believe it is generally applicable, *i.e.*, can be utilized for a variety of treatment systems. The fluence model allows calculation of kerma and absorbed dose, which are measurable quantities, facilitating validation and calibration. This approach also helps us separately calculate the physical and the biological aspects of neutron exposures, i.e., it provides a method to calculate absorbed dose, rather than equivalent dose which takes into account neutron quality, which is challenging in radiation therapy exposures. For these reasons, our model could enable risk calculations in prospective and retrospective cases, providing a potentially powerful tool for designing and conducting epidemiology studies and clinical trials.

The results from this work are generally consistent with the findings from previous studies. Perez-Andujar et al. (2013) found that analytical models of neutron exposure required 49 parameters to predict equivalent dose. Schneider et al. (2015) subsequently improved the model

from Perez-Andujar et al. (2013) reducing the required number of parameters to 22. In comparison, our analytical model with just 40 parameters calculates numerous quantities with reasonable accuracy. Thus, our model is similarly parsimonious but with the capability to predict more quantities ($\Phi(E_{\mathrm{n}})$, Φ_{n}, K, D), albeit at lower accuracy than that reported by Perez-Andujar et al. (2013). Recently, Dommert et al. (2017) reported a neutron spectral fluence model but with less resolution of structure above 1 MeV. The approach of Dommert et al. (2017) requires 11 parameters per spectral fluence whereas our model requires 18 parameters per spectral fluence but has higher resolution above 1 MeV. The reported model from Dommert et. al. (2017) did not explicitly account for proton beam energy, neutron source position, fluence divergence and attenuation. In contrast, our neutron spectral fluence model uses 30 parameters and predicts spectra at all the locations in a water phantom for wide range of energies. Additional, we explicitly modeled source position, attenuation, source distribution.

This project has several strengths. We used a vast amount of high quality radiometric data to train our model. Further, our model uses relatively simple physics-based theories, that provide good explanatory power. Additionally, we modeled the intermediate quantities neutron spectral fluence and kerma rather than dose equivalent. $\phi(E_{\mathrm{n}})$ and D can be directly confirmed by radiation measurements, e.g., in the reference field at a standards laboratory. Being able to calculate $\phi(E_{\mathrm{p}}, x, y, z)$ gives valuable information about the radiation quality (e.g., mean neutron energy) and allows for material dependence in kerma and absorbed-dose calculations.

A limitation of this work is that physics of radiation transport near the surface of phantom is more complex than our spectral fluence model takes into account, as evidenced by relatively poor agreement in some surface regions. Another limitation of the study is that it only uses MC simulated data, *i.e.*, no measurements were used. This is not a major limitation because the MC

code was previously benchmarked extensively in the literature. Additionally, we used only a water-box phantom data and thus we have not tested its capabilities in anatomic phantoms. This is not a serious limitation because the goal of this project is to investigate the feasibility of modeling the underlying transport physics in a simple phantom.

Future work should include study of the physics of neutron transport to improve accuracy in absorbed dose, especially near the phantom surfaces, extend the energy interval to lower proton beam energies (~ 50 MeV) for ocular treatments. Additional work should focus on implementation in treatment planning system and validation against measurements. Finally, computational speed should be investigated because of the large number of calculation points needed for whole-body dose assessments.

Chapter 5. Conclusion

In this work, we developed a physics based analytical model of neutron spectral fluence and an empirical model of neutron kerma coefficients. We combined these to calculate kerma and absorbed dose from stray neutrons. An empirical model of neutron kerma coefficient revealed good agreement with evaluated data from the literature upto 150 MeV. The analytical model for neutron spectral fluence also revealed relatively good agreement with that from MC data. A study of kerma-to-absorbed-dose conversion factor was also performed which suggested it can be approximated as a constant.

The results suggest that it is feasible to use the neutron-fluence-based approach to predict absorbed dose to water from stray neutrons with relatively good accuracy except at shallower depths and far off-axis locations. The results of this work suggest that, with further development and testing, it appears potentially conceivable to perform routine absorbed dose calculation of stray neutron exposure to patients who receive proton beam therapy. A potentially important advantage of this fluence-based approach is that it provides us the ability to take material dependence into account and facilitates characterization of radiation quality of the neutron fields.

References

Agosteo, S., C. Birattari, M. Caravaggio, M. Silari and G. Tosi (1998). "Secondary neutron and photon dose in proton therapy." Radiother Oncol **48**(3): 293-305.

Anferov, V. (2010). "Analytic estimates of secondary neutron dose in proton therapy." Phys Med Biol **55**(24): 7509-7522.

Bonfrate, A., J. Farah, L. De Marzi, S. Delacroix, J. Herault, R. Sayah, C. Lee, W. E. Bolch and I. Clairand (2016). "Influence of beam incidence and irradiation parameters on stray neutron doses to healthy organs of pediatric patients treated for an intracranial tumor with passive scattering proton therapy." Phys Med Biol **32**(4): 590-599.

De Smet, V., M. De Saint-Hubert, N. Dinar, G. P. Manessi, E. Aza, C. Cassell, C. Saldarriaga Vargas, O. Van Hoey, G. Mathot, F. Stichelbaut, G. De Lentdecker, I. Gerardy, M. Silari and F. Vanhavere (2017). "Secondary neutrons inside a proton therapy facility: MCNPX simulations compared to measurements performed with a Bonner Sphere Spectrometer and neutron H*(10) monitors." Radiat Meas **99**: 25-40.

DeSantis, C. E., C. C. Lin, A. B. Mariotto, R. L. Siegel, K. D. Stein, J. L. Kramer, R. Alteri, A. S. Robbins and A. Jemal (2014). "Cancer treatment and survivorship statistics, 2014." CA Cancer J Clin **64**(4): 252-271.

Diallo, I., N. Haddy, E. Adjadj, A. Samand, E. Quiniou, J. Chavaudra, I. Alziar, N. Perret, S. Guerin, D. Lefkopoulos and F. de Vathaire (2009). "Frequency distribution of second solid cancer locations in relation to the irradiated volume among 115 patients treated for childhood cancer." Int J Radiat Oncol Biol Phys **74**(3): 876-883.

Doerr, W. and T. Herrmann (2002). "Second Primary Tumors after Radiotherapy for Malignancies." Strahlenther Oncol **178**: 357-362.

Dommert, M., M. Reginatto, M. Zbořil, F. Fiedler, S. Helmbrecht, W. Enghardt and B. Lutz (2017). "A Bayesian Approach for Measurements of Stray Neutrons at Proton Therapy Facilities: Quantifying Neutron Dose Uncertainty." Radiat Prot Dosim: 1-5.

Eley, J., W. Newhauser, K. Homann, R. Howell, C. Schneider, M. Durante and C. Bert (2015). "Implementation of an analytical model for leakage neutron equivalent dose in a proton radiotherapy planning system." Cancers (Basel) **7**(1): 427-438.

Farah, J., A. Bonfrate, L. De Marzi, A. De Oliveira, S. Delacroix, F. Martinetti, F. Trompier and I. Clairand (2015). "Configuration and validation of an analytical model predicting secondary neutron radiation in proton therapy using Monte Carlo simulations and experimental measurements." Phys Med Biol **31**(3): 248-256.

Farah, J., F. Martinetti , R. Sayah, V. Lacoste, L. Donadille, F. Trompier, C. Nauraye, L. De Marzi, I. Vabre, S. Delacroix, J. Hérault and I. Clairand (2014). "Monte Carlo modeling

of proton therapy installations: a global experimental method to validate secondary neutron dose calculations." Phys Med Biol **59**(11): 2747.

Fontenot, J. D., W. Newhauser and U. Titt (2005). "Design tools for proton therapy nozzles based on the double-scattering foil technique." **116**: 211-215.

Gallagher, K. and P. Taddei (2018). "Independent application of an analytical model for secondary neutron equivalent dose produced in a passive-scattering proton therapy treatment unit." Phys. Med. Biol. **63**(15): 15NT04.

Hendricks, J. S., G. W. McKinney, J. W. Durkee, J. P. F. Finch, M.L., M. R. J. James, R.C., D. B. Pelowitz, L. S. Waters and F. X. Gallmeier (2006). MCNPX, Version 26c; Los Alamos National Laboratory: Los Alamos, NM, USA.

Herault, J., N. Iborra, B. Serrano and P. Chauvel (2005). "Monte Carlo simulation of a protontherapy platform devoted to ocular melanoma." **32**: 910-919.

Hongyu, J., W. Brian, X. G. Xu, D. S. Herman and P. Harald (2005). "Simulation of organ-specific patient effective dose due to secondary neutrons in proton radiation treatment." Phys Med Biol **50**(18): 4337.

Howell, R. M., E. A. Burgett, D. Isaacs, S. G. Price Hedrick, M. P. Reilly, L. J. Rankine, K. K. Grantham, S. Perkins and E. E. Klein (2016). "Measured neutron spectra and dose equivalents from a mevion single-room, passively scattered proton system used for craniospinal irradiation." Int J Radiat Oncol Biol Phys **95**(1): 249-257.

Howlader, N., A. M. Noone, M. Krapcho, J. Garshell, D. Miller and S. F. Altekruse (2014). "SEER cancer statistics review, 1975-2011,report." National Cancer Institute.

ICRU (2000). International Commission on Radiation Units and Measurements. *"Nuclear Data for Neutron and Proton Radiotherapy and for Radiation Protection"* ICRU 63. J. ICRU, (Bethesda, MD: International Commission on Radiation Units and Measurements).

ICRU (2014). International Commission on Radiation Units and Measurements. *"Key Data for Ionizing-Radiation Dosimetry: Measurement Standards and Applications"* ICRU 90. J. ICRU **14**, (Oxford University Press, Oxford).

Islam, M. R., Y. Zheng, T. L. Collums, J. M. Monson, S. Ahmad and E. R. Benton (2017). "Measurement and simulation of secondary neutrons from uniform scanning proton beams in proton radiotherapy." Radiat Meas **96**: 8-18.

Koch, N., W. Newhauser, U. Titt, D. Gombos, K. Coombes and G. Starkschall (2008). "Monte Carlo calculations and measurements of absorbed dose per monitor unit for the treatment of uveal melanoma with proton therapy." Phys Med Biol **53**: 1581-1594.

NCRP (2011). Second primary cancers and cardiovascular disease after radiation therapy: NCRP Report No. 170. . NCRP Publication, Bethesda, MD.

Newhauser, W., J. Fontenot, Y. Zheng, J. Polf, U. Titt, N. Koch, X. Zhang and R. Mohan (2007). "Monte Carlo simulations for configuring and testing an analytical proton dose-calculation algorithm." **52**: 4569-4584.

Newhauser, W. D., C. Schneider, L. Wilson, S. Shrestha and W. Donahue (2017). "A review of analytical models of stray radiation exposures from photon- and proton-beam radiotherapies." Radiat Prot Dosim: 1-7.

Newhauser, W. D., U. Titt, D. Dexheimer, X. Yan and S. Nill (2002). "Neutron shielding verification measurements and simulations for a 235-MeV proton therapy center." Nucl Instrum Meth A **476**(1-2): 80-84.

NRC (2006). Health Risks from Exposure to Low Levels of Ionizing Radiation: BEIR VII Phase 2. Washington, DC, The National Academies Press**:** 422.

Perez-Andujar, A., R. Zhang and W. Newhauser (2013). "Monte Carlo and analytical model predictions of leakage neutron exposures from passively scattered proton therapy." Med Phys **40**(12).

Polf, J. C. and W. D. Newhauser (2005). "Calculations of neutron dose equivalent exposures from range-modulated proton therapy beams." Phys Med Biol **50**(16): 3859-3873.

Schneider, C., W. Newhauser and J. Farah (2015). "An analytical model of leakage neutron equivalent dose for passively-scattered proton radiotherapy and validation with measurements." Cancers **7**(2): 795-810.

Siegel, R., K. Miller and A. Jemal (2018). Cancer statistics, 2018, Surveillance, Epidemiology, and End Results (SEER) CA Cancer J clin. **68**.

Smart, D. R. (2010). Physician Characteristics and Distribution in the U.S. Chicago,IL, Division of Survey and Data Resources.

Tayama, R., Y. Fujita, M. Tadokoro, H. Fujimaki, T. Sakae and T. Terunuma (2006). "Measurement of neutron dose distribution for a passive scattering nozzle at the Proton Medical Research Center (PMRC)." Nucl Instrum Meth A **564**(1): 532-536.

Tayama, R., H. Handa, K. Hayashi, H. Nakano, N. Sasamoto, H. Nakashma and F. Masukawa (2002). "Benchmark calculations of neutron yields and dose equivalent from thick iron target for 52–256 MeV protons." **213**: 119-131.

Trinkl, S., V. Mares, F. S. Englbrecht, J. J. Wilkens, M. Wielunski, K. Parodi, W. Ruhm and M. Hillbrand (2017). "Systematic out-of-field secondary neutron spectrometry and dosimetry in pencil beam scanning proton therapy." Med Phys **44**(5): 1912-1920.

Tukenova, M., C. Guibout, O. Oberlin, F. Doyon, A. Mousannif, N. Haddy, S. Guerin, H. Pacquement, A. Aouba, M. Hawkins, D. Winter, J. Bourhis, D. Lefkopoulos, I. Diallo and F. de Vathaire (2010). "Role of cancer treatment in long-term overall and cardiovascular mortality after childhood cancer." J Clin Oncol **28**(8): 1308-1315.

Williams, J. and W. Newhauser (2018). "Normal tissue damage: its importance, history and challenges for the future." BJR **(at press)**.

Williams, T., C. Kelly and a. m. others (2017). "GNUPLOT Version 5.2 patchlevel 0 Copyright (c) 1986-1993, 1998, 2004, 2007-2017."

Yan, X., U. Titt, A. M. Koehler and W. D. Newhauser (2002). "Measurement of neutron dose equivalent to proton therapy patients outside of the proton radiation field." Nucl Inst Meth A **476**(1-2): 429-434.

Zhang, R., J. Fontenot, D. Mirkovic, J. Hendricks and W. Newhauser (2013). "Advantages of Mcnpx-Based Lattice Tally over Mesh Tally in High-Speed Monte Carlo Dose Reconstruction for Proton Radiotherapy." Nucl Technol **183**(1): 101-106.

Zhang, R., A. Perez-Andujar, J. D. Fontenot, P. J. Taddei and W. D. Newhauser (2010). "An analytic model of neutron ambient dose equivalent and equivalent dose for proton radiotherapy." Phys Med Biol **55**(23): 6975-6985.

Zheng, Y., J. Fontenot, P. Taddei, D. Mirkovic and W. Newhauser (2008). "Monte Carlo simulations of neutron spectral fluence, radiation weighting factor and ambient dose equivalent for a passively scattered proton therapy unit." Phys Med Biol **53**(1): 187-201.

Vita

Suman Shrestha was born in Biratnagar, Nepal and moved to capital city Kathmandu when he turned one, where he was raised before graduating from Amrit Science College with a Bachelor in Science degree in Physics in 2010. Suman then enrolled in Central Department of Physics, Tribhuvan University for Master in Science degree in Physics and graduated in September 2013. Following graduation Suman worked as a physics lecturer in National Institute of Science and Technology, Lainchour, Kathmandu for 1.5 years before pursuing higher education in USA. In 2015, he entered the LSU Medical & Health Physics Graduate Program in Baton Rouge, Louisiana as a Master's candidate. He expects to graduate with a Master of Science degree in medical physics in Fall 2018. Upon completion of his master's degree, he will begin work on his doctorate at The University of Texas MD Anderson Cancer Center, Houston, Texas.